mSWI/SNF promotes distal repression by titrating polycomb dosage

Christopher M. Weber[1,2], Antonina Hafner[2], Simon M. G. Braun[1,2], Alistair N. Boettiger[2], and Gerald R. Crabtree[1-3]
1) Department of Pathology 2) Developmental Biology, Stanford University School of Medicine, Stanford, California, USA.
3) Howard Hughes Medical Institute, Chevy Chase, Maryland, USA.
*Correspondence should be addressed to G.R.C. (crabtree@stanford.edu)

Abstract

The mammalian SWI/SNF, or BAF complex, has a conserved and direct role in antagonizing polycomb-mediated repression. Yet, BAF appears to also promote repression by polycomb in stem cells and cancer. How BAF both antagonizes and promotes polycomb-mediated repression remains unknown. Here, we utilize targeted protein degradation to dissect the BAF-polycomb axis in embryonic stem cells on the timescale of hours. We report that rapid BAF depletion leads to quick redistribution of both PRC1 and PRC2 complexes from highly occupied domains, like Hox clusters, to weakly occupied sites genome-wide. This results in transcriptional derepression, chromatin decompaction, and opposite epigenomic changes to repressed domains. Surprisingly, we find that limiting polycomb dosage underlies these effects, such that BAF driven polycomb antagonism titrates the dosage required for repression, reconciling the opposing roles. These findings provide an explanation for the frequent mutation of BAF subunits in neurodevelopmental disorders and certain cancers.

Keywords: transcriptional regulation; ATP-dependent chromatin remodeling; SWI/SNF complex; polycomb; PRC1; PRC2; Hox genes, targeted protein degradation; degron.

Introduction

Chromatin regulation is critical to establish and maintain the precise gene expression states that define cellular identity and prevent human pathologies (Flavahan et al., 2017). The balance between different states primarily involves the antagonism between activating (Trithorax-group) and repressive (Polycomb-group) proteins (Schuettengruber et al., 2017). Opposition between these two classes of chromatin regulators was first demonstrated genetically during Drosophila development (Kingston and Tamkun, 2014). For example, deletion of Polycomb-group genes results in Hox gene derepression which gives rise to homeotic transformations, whereas Trithorax-group mutations dominantly suppress these phenotypes (Kennison and Tamkun, 1988; Tamkun et al., 1992). Similarly, loss of function mutations in Trithorax-group genes also produce homeotic transformations but are instead due to insufficient Hox gene expression (Capdevila et al 1981). Following these pioneering studies, the genes encoding members of these groups have been shown to be mutated in many human diseases. This is especially true for the BAF (mSWI/SNF) complex, a Trithorax-group homolog, which is frequently mutated in many cancers, neurodevelopmental disorders, and intellectual disabilities (Kadoch and Crabtree, 2013; Ronan et al., 2013; Shain and Pollack, 2013).

BAF complexes are combinatorially assembled chromatin remodeling enzymes of ~15 subunits that hydrolyze ATP to mobilize nucleosomes and generate accessible DNA (Clapier et al., 2017). In mammalian cells, BAF directly evicts both polycomb repressive complexes (PRC) 1 and 2 (Kadoch et al., 2017; Stanton et al., 2017) leading to transcriptional derepression (Braun et al., 2017). Thus, the ability of Trithorax-group proteins to antagonize polycomb-mediated repression is conserved from Drosophila to mammals. PRC1 and PRC2 direct H2A ubiquitination (H2AK119ub1) and trimethylation of histone H3 at lysine 27 (H3K27me3) respectively and spatially constrain the genome in support of transcriptional repression (Schuettengruber et al., 2017). BAF-mediated polycomb antagonism is essential during development and is thought to underlie the tumor suppressive role in human cancers (Valencia and

Kadoch, 2019). Conversely, BAF's potent ability to antagonize polycomb-mediated repression is coopted in synovial sarcoma, where translocation of SSX onto the SS18 subunit retargets BAF and opposes polycomb-mediated repression to drive tumor growth (Kadoch and Crabtree, 2013; McBride et al., 2018).

Despite extensive evidence that BAF has a dominant role in polycomb opposition, BAF appears to also be required for polycomb-mediated repression in embryonic stem cells, during lineage commitment, and in sub-types of rare atypical teratoid rhabdoid tumors (ATRT) that are characterized by Hox gene derepression (Alexander et al., 2015; Ho et al., 2011; Johann et al., 2016). ATRTs are highly malignant tumors that are typically seen in children younger than 3. These tumors are characterized by inactivation of either BAF47 or Brg1, the core ATPase subunit, and rarely contain mutations in other genes (Masliah-Planchon et al., 2015; Nakayama et al., 2017). Currently, the mechanism by which BAF can simultaneously support active and repressed states remains unknown.

A major limitation to resolving this question has been with loss of function approaches that lack sufficient temporal resolution. Chromatin remodeling complexes like BAF regulate accessibility for virtually all DNA-based processes and have many ascribed roles from transcriptional regulation to cell division. Additionally, chromatin regulators tend to be stable for several days following conditional deletion or knockdown and are subject to feedback mechanisms, making it impossible to determine whether transcriptional effects are primary or secondary. To overcome these limitations, we implemented a chemical genetic approach to enable rapid targeted protein degradation of BAF, PRC1, and PRC2 in mouse embryonic stem cells (mESCs). We demonstrate that BAF inactivation results in the genome-wide redistribution of PRC1 & 2 on the timescale of hours, from highly occupied domains like Hox clusters, to sites that are normally lowly occupied. Moreover, we demonstrate through both dose-dependent degradation of PRC1&2 and PRC1 overexpression that insufficient polycomb dosage underlies these effects. Collectively, our study reveals that BAF titrates the dosage of PRC1&2 complexes on chromatin, reconciling the dual role for BAF in opposition and maintenance of polycomb-mediated repression.

Results

Brg1 degradation with auxin is rapid and near complete

To temporally resolve the downstream effects of BAF inactivation we developed an ESC line where the core ATPase subunit Brg1 (also known as Smarca4) can be rapidly degraded. Both endogenous alleles of Brg1 were tagged with the minimal 44 amino acid auxin inducible degradation tag (AID*) using CRISPR-Cas9 with homology-dependent repair (Morawska and Ulrich, 2013; Nishimura et al., 2009) (Supplementary Fig 1A,B). The F-box protein osTIR1 was inducibly expressed in these cells, which forms a hybrid SCF ubiquitin ligase complex that targets Brg1 for degradation by the proteasome when the small molecule auxin is added (Figure 1A). Tagging Brg1 with AID* did not affect protein abundance, such that for all experiments Brg1 levels were equivalent to WT before the addition of auxin (Figure 1B). Additionally, these cells divide at the same rate and appeared indistinguishable from the parent mESC line. Consistent with other studies, auxin addition in the absence of osTIR1 was innocuous to cell viability and growth (Nora et al., 2017). Yet, when auxin was added to cells expressing osTIR1, Brg1 was rapidly degraded, with a protein half-life of ~30 minutes and maximal, near-complete, degradation was achieved by 2 hours (Figure 1C). A degron approach enables much faster loss of function compared to genetic deletion which takes ~3 days for comparable protein depletion. This induces much faster disruption to colony morphology and a reduction in peripheral alkaline phosphatase staining at 24h, indicative of compromised pluripotency (Figure 1D, and Supplementary Figure 1C). Thus, the Brg1 degron is a tractable and robust strategy to resolve the effects of BAF inactivation on the timescale of hours.

Brg1 degradation results in the derepression of many highly polycomb bound genes

Previous studies have shown that genetic deletion or knockdown of Brg1 results in differential expression

of many genes after 3-4 days (Ho et al., 2009; Ho et al., 2011; Stanton et al., 2017). These time-points are unable to capture primary effects and likely combine secondary changes driven by a small number of primary genes. To define the primary effects of rapid Brg1 depletion on transcription, we conducted an RNA-seq time-course at 2, 4, 8, and 24 hours. We observed differential expression changes at the earliest 2-hour time-point, when Brg1 degradation has just reached the maximal level. The number of differentially expressed genes increased at each successive time-point, with n = 788 upregulated and n = 842 downregulated genes at 24-hours (FDR-corrected $P < 0.05$) (Figure 2A). There was a high degree of overlap between differentially expressed genes at each time-point (Supplementary Figure 2A, B) revealing that instead of oscillating waves of transcription, there was a progressive increase in the magnitude of differential expression over time (Figure 2B). Interestingly, the overlap between differentially expressed genes in genetic deletion studies and Brg1 degradation was modest (Supplementary Figure 2C), suggesting that rapid depletion captured a distinct, more direct effect from other approaches. Thus, Brg1 degradation induces quick transcriptional changes, both up and down, that progressively increase in magnitude over the time-course, consistent with being directly regulated by BAF.

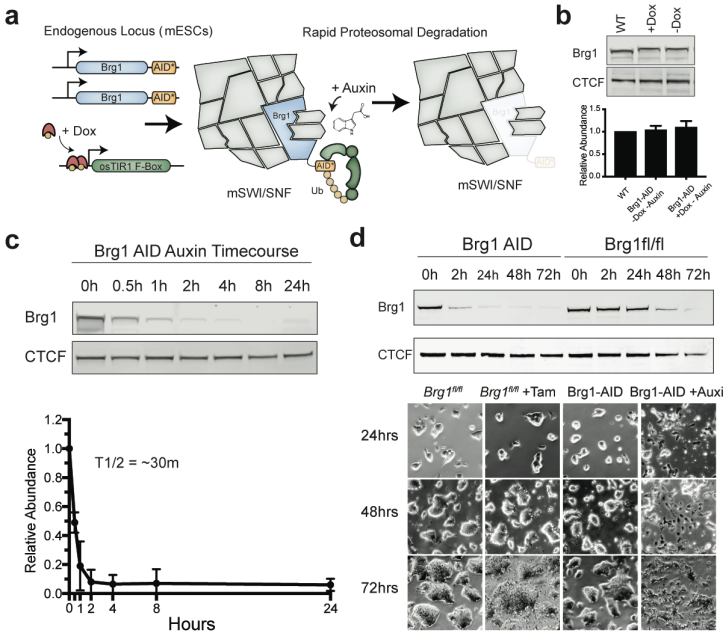

Figure 1: Brg1 degradation with auxin is rapid and near complete
(a) Schematic depicting Brg1 auxin inducible degradation (AID) strategy in mESCs. Both alleles of Brg1 are endogenously tagged at the C-terminus with the minimal AID* tag. osTIR1 is induced by doxycycline before adding auxin to degrade Brg1. (b) Representative western blot and quantitation of Brg1 abundance in parent line compared to Brg1-AID* +/- osTIR1 induction (-auxin). Error bars represent mean +/- standard deviation from five biological replicates. (c) Representative western blot and quantitation of Brg1 AID time-course. Error bars represent mean +/- standard deviation from three biological replicates. (d) Comparison of Brg1 depletion kinetics between AID and Cre-lox genetic deletion by western blot and colony morphology. Cells were only grown on the same dish for 72h to illustrate timing for Brg1 $^{fl/fl}$ colony morphology changes.

We were surprised to find that many of the most strongly derepressed genes colocalized with major PRC1 and PRC2 peaks with the highest occupancy on the chromosome (Figure 2C). Many Polycomb-group target genes in ES cells have roles in neural development (Boyer et al., 2006). Consistent with this, upregulated genes were strongly enriched for neural differentiation genes and neural transcription factors (Supplementary Figure 2D). Hox A, B, and D genes were amongst the most strongly derepressed (up to ~440 fold by 24h) and showed a clear time-dependent increase in transcription upon Brg1 degradation with changes seen as early as the 2-hour time-point (Figure 2D, E). Previous studies have shown that some of these sites form extra long-range chromosomal interactions that require PRC1, (indicated by dashed arrows in Fig 2C), for example between HoxD and Bmi1, Pax6, Meis2, and Lmx1b. These contacts are lost when cells are switched to 2i media, resembling a more naïve pluripotent state that is less reliant on polycomb-mediated repression (Joshi et al., 2015). We compared Brg1 degron mediated derepression in 2i vs serum conditions and found that the effect was much stronger in serum (~3 to 16 fold for Hox genes) consistent with compromised polycomb-mediated repression driving the transcriptional derepression (Supplementary Figure 2E).

Collectively, these results suggest that BAF directly facilitates polycomb-mediated repression. Consistent with this model, we found that many genes that were derepressed by Brg1 degradation were also derepressed upon knockout of PRC1&2 (349 of 788) (King et al., 2018). In addition, these genes showed

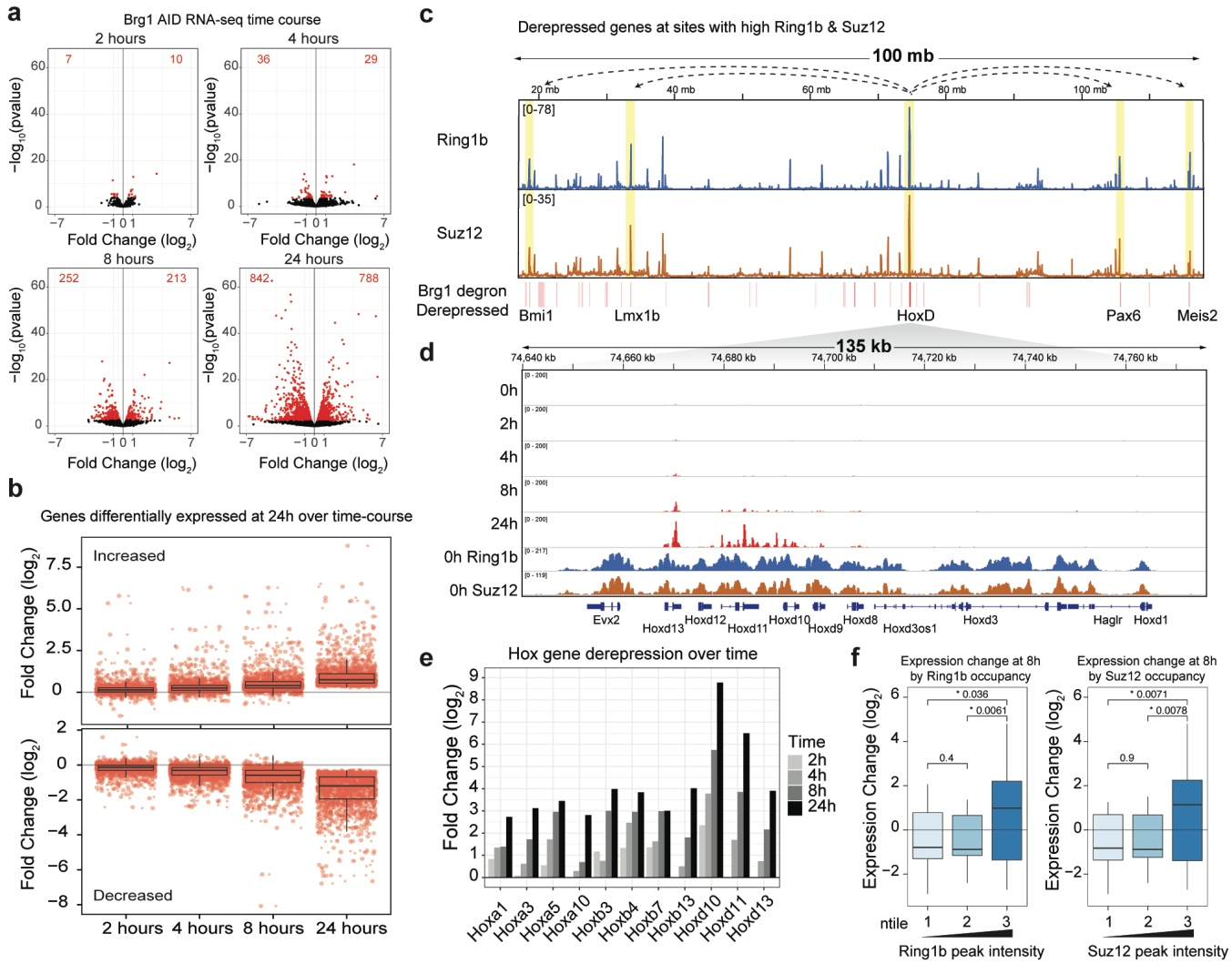

Figure 2: Brg1 degradation results in the derepression of many highly polycomb-bound genes
(a) Volcano plots depicting gene expression changes at 2, 4, 8, and 24 hours of Brg1 degradation. Differentially expressed genes are colored red (FDR-corrected $P < 0.05$) from two biological replicates for each time-point. (b) Log_2 fold change for genes that are differentially expressed at 24h (FDR-corrected $P < 0.05$) across all time-points (increased n=788, decreased n=842). (c) Browser tracks showing Ring1b and Suz12 ChIP-seq signal at 100mb of 181mb long chromosome 2 and a heatmap of significantly derepressed genes at 24h of Brg1 degradation (bottom). A few regions are highlighted in yellow that have high polycomb occupancy, form extra-long range contacts with HoxD, and become derepressed by Brg1 degradation. (d) Browser snapshot of HoxD locus (130kb) with Suz12, Ring1b, and RNA-seq tracks. (e) Log_2 fold change of Hox genes that are differentially expressed across the time-course (HoxA, B, and D clusters). (f) Differentially expressed genes at 8h Brg1 degradation that contain a Ring1b or Suz12 peak +/- 2kb from gene transcription start site by ntile of ChIP-seq peak intensity. t-test p-value is shown.

a similar time-dependent increase in transcription following Brg1 degradation, consistent with being directly regulated and not due to a far downstream consequence of losing a key repressor or upregulation of an activator (Supplementary Figure 2F, G). Considering that many genes with high polycomb occupancy became derepressed, like the Hox clusters, we next investigated differential expression with respect to polycomb occupancy. Looking at 8h, an intermediate timepoint where ~450 of ~1600 total genes are differentially expressed, we found a negative correlation between polycomb occupancy and differential expression upon Brg1 degradation. Genes that were lowly bound by polycomb (Ring1b or Suz12 peaks +/- 2kb from the TSS, ntiles 1 and 2) became repressed, whereas genes with the highest polycomb levels (ntile 3) were derepressed by Brg1 degradation (Figure 2F, $P < 0.05$ between ntiles 1,2 and 3 for both Ring1b and Suz12). This temporally resolved loss of function approach demonstrates that rapid BAF inactivation has opposing effects on polycomb-mediated gene regulation, that depends on the initial level of polycomb occupancy.

PRC1 and PRC2 are quickly redistributed upon Brg1 degradation

We next sought to determine the effect of Brg1 degradation on PRC1&2 occupancy genome-wide by conducting ChIP-seq for Ring1b and Suz12 (core components of PRC1 and PRC2 complexes) (Supplementary Fig 3A). Consistent with the established role for BAF in polycomb eviction, we found that more Ring1b and Suz12 peaks increased than decreased upon 8h of Brg1 degradation (931 increased, 641 decreased, 1,572/10,569 14.9% of peaks changed and 457 increased, 200 decreased 657/8,853, 7.4% of peaks changed for Ring1b and Suz12 respectively at FDR-corrected $P < 0.1$). Peaks with low Ring1b and Suz12 occupancy were mostly increased (as assessed by normalized peak counts), whereas highly occupied peaks mostly showed loss following 8h Brg1 degradation (Figure 3A). This general trend can be seen in representative genome-browser snapshots of increased (Cyp2s1 and Ptk2b) and decreased (HoxA/D clusters) sites (Figure 3B) (Supplementary Figure 3B, C). We next sought to better temporally resolve this loss at heavily occupied loci, since it's currently unclear how BAF might promote polycomb-mediated repression at these sites. We conducted Ring1b ChIP-qPCR at additional time-points (4, 8, and 24h). All sites assayed showed significant loss by 4 hours, that decreased in a time-dependent manner (~20-60% reduction), further supporting a direct time-dependent requirement on BAF activity (Supplementary Figure 3D). Collectively, these results demonstrate that the loss of PRC2 at Hox clusters previously seen after 72h conditional deletion (Ho et al., 2011) occurs after only a few hours and revealed

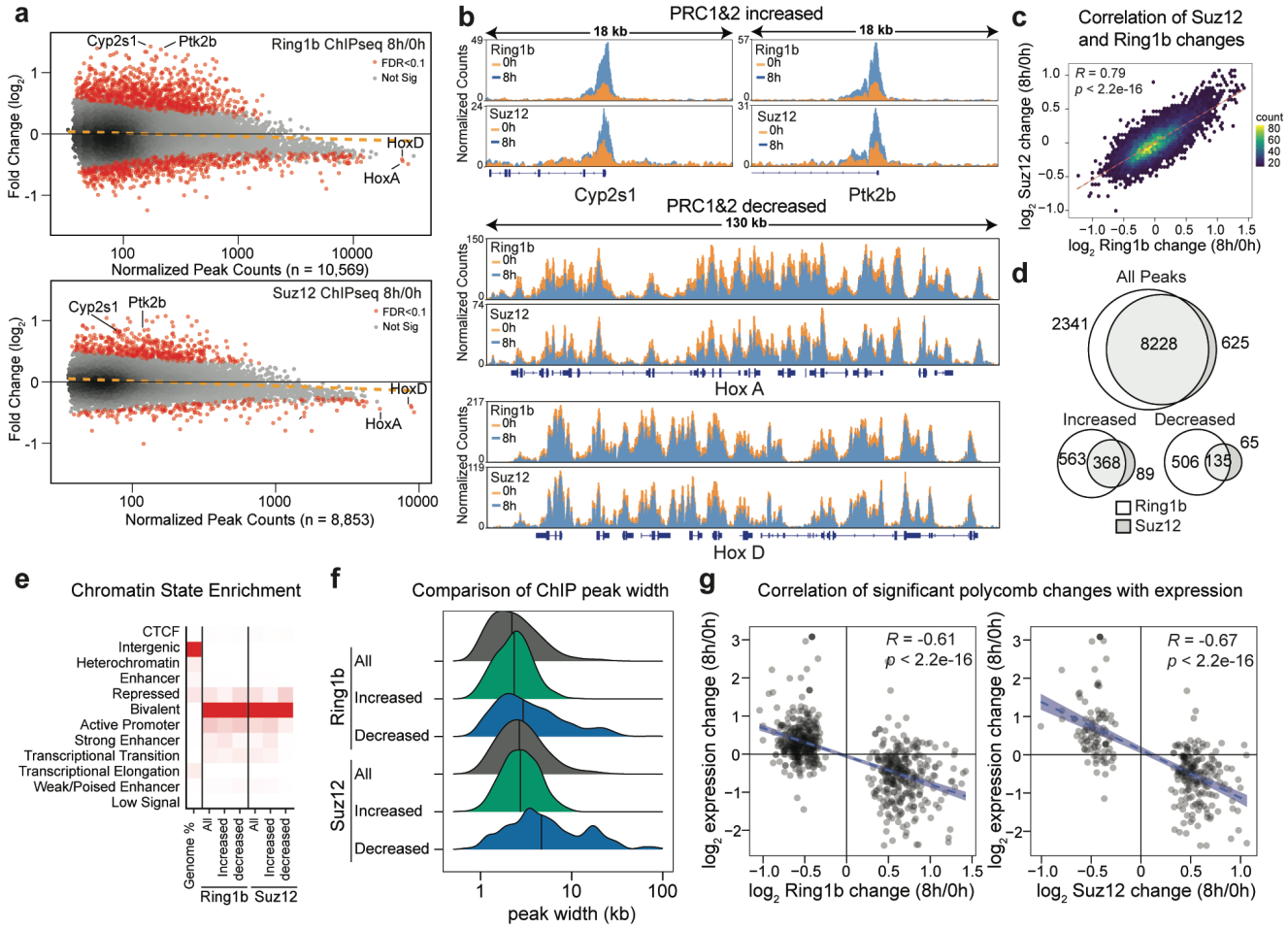

Figure 3: PRC1 and PRC2 are quickly redistributed upon Brg1 degradation

(a) MA plot showing genome-wide changes to Ring1b and Suz12 ChIP-seq peaks (n = 10,569 and n = 8,853 respectively) at 8h Brg1 degradation with differentially bound peaks in red (FDR-corrected P < 0.1) from four biological replicates. For Ring1b, there are n = 930 increased and n = 640 decreased peaks, and for Suz12 there are n = 457 increased and n = 198 decreased peaks. (b) Representative genome-browser tracks for peaks labeled in (a) that increase (Cyp2s1 and Ptk2b) and decrease (HoxA and HoxD clusters) normalized by read-depth. (c) Correlation plot between Ring1b and Suz12 peak changes as a hexagonal heatmap of 2D bin counts. Correlation and p-values were obtained from Pearson's product moment correlation. (d) Peak overlap for all, increased, and decreased between Ring1b and Suz12. (e,f) chromatin state enrichment and peak widths for all, increased, and decreased peak changes for Ring1b and Suz12. (g) Correlation of significantly changed Ring1b and Suz12 peaks that are +/- 2kb from gene transcription start sites and gene expression changes at 8h Brg1 degradation. Correlation and p-values were obtained from Pearson's product moment correlation.

that PRC1 is also lost. In fact, Brg1 degron induced changes to PRC1&2 were highly correlated across all peaks (R = 0.79, p < 2.2e-16) and differentially bound peaks displayed a high degree of overlap (Figure 3C,D). Importantly, these changes were independent of global changes to the histone modifications placed by these complexes and the core proteins themselves even at much longer time-points (Supplementary Figure 3E).

Chromatin state enrichment analysis (Ernst and Kellis, 2012) revealed that PRC1&2 peaks were highly enriched for bivalent chromatin, with slight enrichment for the repressed state in sites decreased upon Brg1 degradation (Figure 3E). We wondered whether the high normalized peak counts seen at decreased sites were due to enrichment for broader domains as a general principle, as seen for the Hox clusters, so we plotted the peak width density for all, increased, and decreased peaks (Figure 3F). We found that the increased peaks had a very similar distribution to all PRC1&2 peaks (Ring1b median for all peaks = 2.2kb, increased = 2.3kb and Suz12 median for all peaks = 2.9kb, increased = 2.7kb), but decreased peaks contained broader polycomb domains (Ring1b median decreased = 2.9kb, Suz12 median decreased = 4.7kb). We previously showed that the basal occupancy level of PRC1&2 was predictive of the direction of differential gene expression when Brg1 was degraded (Figure 2F). So, we next sought to determine how global polycomb changes influence transcription at the same 8h time-point. We found that for all genes, there was a modest but highly significant negative correlation between changes to polycomb and transcription (Supplementary Fig 3F, Ring1b: R = -0.29, P < 2.2e-16, Suz12: R= -0.31, P < 2.2e-16). Yet, considering only Brg1-dependent peaks, we observed a much stronger negative correlation (R = -0.61, P < 2.2e-16 and R = -0.67, P < 2.2e-16 for Ring1b and Suz12 respectively). Altogether, these results demonstrate that Brg1 degradation induces the genome-wide redistribution of both PRC1 and PRC2 away from highly occupied broad peaks towards smaller peaks at bivalent chromatin, which leads to opposing effects on transcription output.

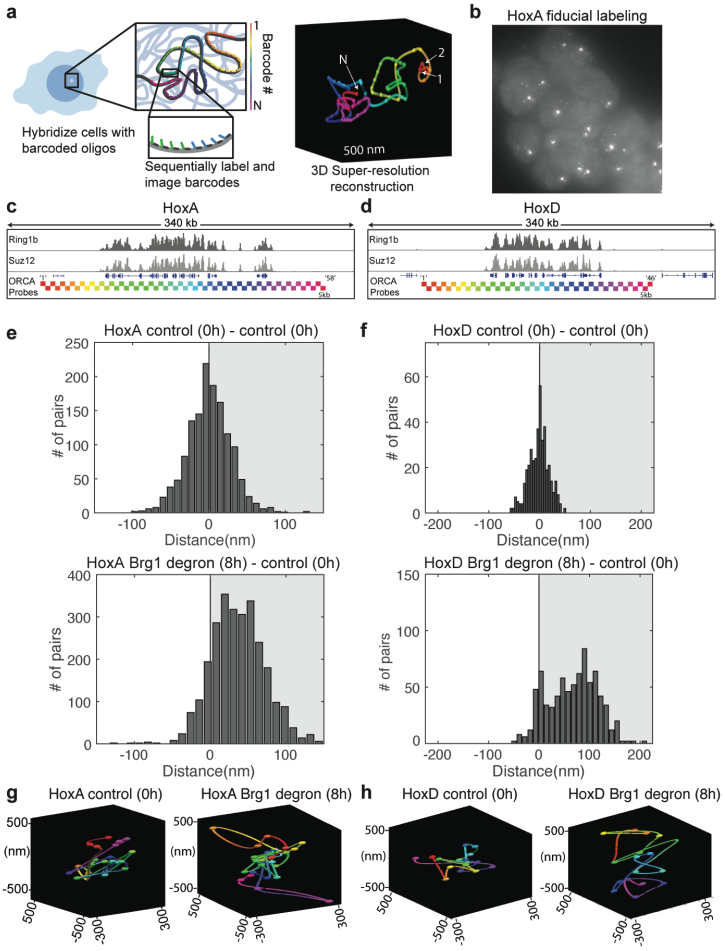

Figure 4: Brg1 degradation and polycomb loss result in decompaction of HoxA and HoxD regions
(a) Schematic of ORCA method where sequential imaging and labeling of fluorescent barcodes (numbers 1 to N) are artificially color coded by barcode number, enabling reconstruction of the 3D DNA path of a DNA region. (b) mES cells labelled with HoxA probe. Each spot corresponds to one allele and shown here is the fiducial staining, that labels the entire 290kb HoxA region. c,d) Genomic HoxA and HoxD regions labelled by ORCA. Bottom tracks illustrate the positions of probes, color coded by barcode number. (e,f) Histograms plot the difference in median distance for all barcode pairs, where median was calculated over all cells, between AID treated and control cells. (g,h) Representative polymers in the control and Brg1 depleted cells for HoxA (g) and HoxD (h).

Brg1 degradation and polycomb loss result in decompaction of Hox

Polycomb complexes are known to constrain and physically compact chromatin, which is thought to facilitate repression (Boettiger et al., 2016; Eskeland et al., 2010; Francis et al., 2004), leading us to ask if the PRC1&2 loss from high polycomb occupancy sites is sufficient to spatially decompact them. To test this, we conducted ORCA experiments (Optical Reconstruction of Chromatin

Architecture) (Bintu et al., 2018; Boettiger et al., 2016; Mateo et al., 2019) at HoxA and HoxD clusters, which lose polycomb and become transcriptionally derepressed by Brg1 degradation. ORCA enables reconstruction of chromatin trajectories (100-700kb) by tiling short regions (2-10kb) with unique barcodes and measuring their nanoscale 3D positions (Figure 4A,B). We tiled 290kb at HoxA and 234kb at HoxD in 5kb steps, i.e. different barcode for each 5kb step, that completely cover the polycomb repressed domains and extend into the flanking regions (Figure 4C,D).

Applying ORCA in the untreated cells, and calculating the contact frequency over all cells revealed similar sub-TAD domain architecture and a high correlation with published Hi-C data in mESCs (Bonev et al., 2017) (Supplementary Figure 4A, B). We then leveraged the unique ability of ORCA to measure 3D nanoscale distances and quantified the median inter-barcode distance at HoxA and HoxD following Brg1 degradation. We found higher inter-barcode distances for both HoxA and HoxD when Brg1 is degraded (8h) (Figure 4E, F, Supplementary Figure 4C, D) which is also apparent in the re-constructed polymer traces from single cells (Figure 4G,H). Thus, the redistribution of polycomb away from Hox clusters is sufficient to spatially decompact them.

Genome-wide polycomb changes after Brg1 degradation result in opposite changes to active chromatin features

Transcriptional regulation involves a dynamic interplay between activating and repressive forces. We next sought to determine how the genome-wide redistribution of polycomb-mediated repression impacts other chromatin features associated with active transcription. We conducted ChIP-seq for H3K4me3 and H3K27ac following 8h Brg1 degradation. H3K4me3 is a histone modification associated with poised and transcriptionally active genes that is deposited by the COMPASS complex, which has homologous subunits in Drosophila that are Trithorax-group members, like the BAF complex (Piunti and Shilatifard, 2016). H3K27ac is primarily deposited at active genes and enhancers by the CBP/p300 complex and antagonizes the H3K27me3 modification that is placed by PRC2 (Tie et al., 2009). Interestingly, we found that at 8h Brg1 degradation, both H3K27ac and H3K4me3 were negatively correlated with changes to Ring1b (R = -0.45, P < 2.2e-16 and R = -0.5, P < 2.2e-16) and Suz12 (R = -0.37, P < 2.2e-16 and R = -0.44, P < 2.2e-16) genome-wide (Figure 5A,B), such that loci with increased PRC1&2 had decreased active marks (Figure 5C) and loci with decreased PRC1&2 had an increase 8h after Brg degradation (Figure 5D) (Supplementary Figure 5A, B). These results demonstrate that the global polycomb redistribution induced by Brg1 degradation results in converse epigenomic changes associated with active transcription.

We next sought to understand what drives the global redistribution of polycomb from highly occupied sites. One possibility is that BAF inhibits transcription through nucleosome positioning (Hainer et al., 2015) and the act of transcription leads to polycomb loss due to physical disruption from the transcription machinery or by competitive removal through preferential PRC2 binding to RNA (Wang et al., 2017). We tested this idea by blocking transcription initiation with Triptolide for 8h (Bensaude, 2011) (Supplementary Figure 5F). Global transcription inhibition caused much larger changes to polycomb occupancy than Brg1 degradation, affecting 49.7% (6,584/13,226) of Ring1b and 46.9% (6,162/13,147) of Suz12 peaks. These changes showed zero, or very weak correlation with Brg1 deletion, suggesting that BAF regulation of polycomb occupancy is largely independent of transcription (R = 0.01 for Ring1b and R = 0.25 for Suz12) (Supplementary Figure 5G, H). Consistent with this, blocking transcription and degrading Brg1 at the same time, when controlling for global transcriptional inhibition, resulted in a strong positive correlation with Brg1 degradation alone for both Ring1b (R = 0.67, P < 2.2e-16) and Suz12 (R = 0.65, P < 2.2e-16) (Supplementary Figure 5I). These results confirm that polycomb loss following Brg1 degradation is independent of transcription, which is consistent with the loss of polycomb across large

domains, not just near genes that become derepressed.

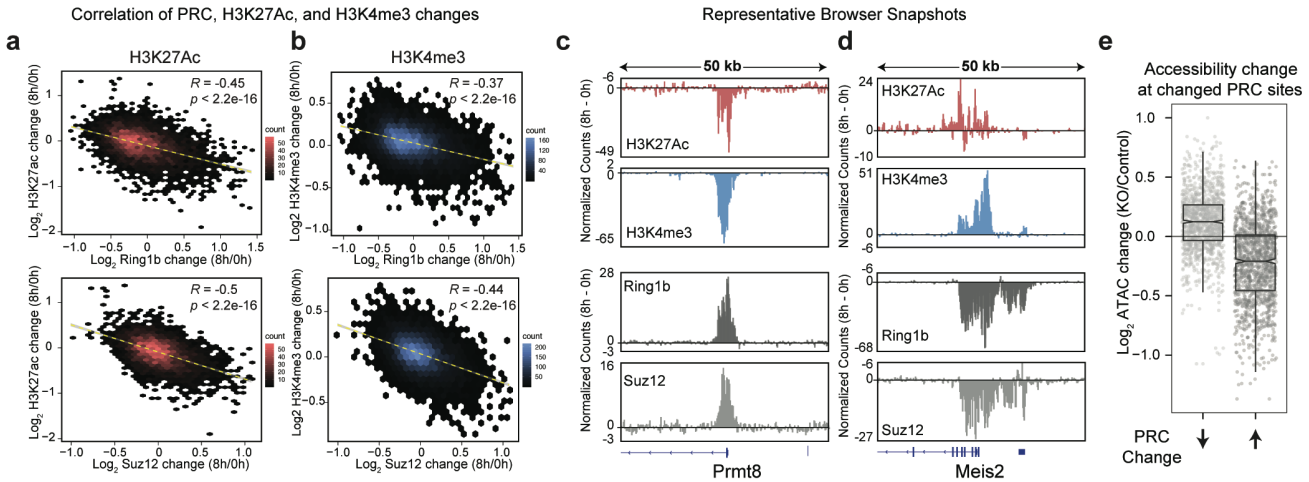

Figure 5: Genome-wide polycomb changes after Brg1 degradation result in opposite changes to active chromatin features
Correlation plot of fold change (Log_2) to H3K27ac (a) H3K4me3 (b) and Ring1b or Suz12 at 8h Brg1 degradation as hexagonal heatmap of 2D bin counts. Correlation and p-values were obtained from Pearson's product moment correlation. (c) Representative browser snapshots showing Prmt8 locus that gains Ring1b and Suz12 and loses both H3K27ac and H3K4me3 as the difference in normalized counts (8h – 0h degradation). (d) Browser snapshot at Meis2 locus which loses Ring1b and Suz12 and gains both H3K27ac and H3K4me3. (e) Boxplot showing the change in accessibility to Tn5 transposition in $Brg^{fl/fl}$ deleted cells (TAM) over control (EtOH), at peaks that have decreased or increased Ring1b or Suz12 signal after 8h Brg1 degradation. (ATAC-seq data from (Miller et al., 2017)).

In general, BAF and PRC1&2 overlap extensively genome-wide, however highly occupied sites are mutually exclusive for both (Supplementary Fig 5C, D). This suggests that BAF antagonizes polycomb at weakly bound sites but is mostly excluded from highly bound sites, like Hox. To investigate this further, we looked at accessibility changes by ATAC-seq that result from Brg1 depletion at sites where polycomb changes (Miller et al., 2017). Accessibility changes likely reflect the most accurate signature of SWI/SNF chromatin remodeling activity since the readout is the endpoint of the catalytic cycle, i.e. nucleosome eviction. We reasoned that if BAF generated accessibility that is required to load polycomb, then accessibility changes should mimic polycomb changes. In sharp contrast to this, we actually found that sites that lost polycomb become more accessible, and sites that gained polycomb become less accessible (Figure 5E, and Supplementary Figure 5C). These changes in accessibility are attributed solely to BAF ATPase activity, as polycomb deletion does not affect accessibility to Tn5 transposition in mESCs (Hodges et al., 2018; King et al., 2018). These results are most consistent with a model where BAF facilitates polycomb-mediated repression through distant PRC1&2 eviction at abundant sites of low polycomb affinity, allowing for accumulation at sites of apparent higher affinity, such as Hox genes.

PRC1&2 dosage sensitivity underlies the requirement for BAF in polycomb-mediated repression

If our model is correct and BAF acts by ATP-dependent eviction of polycomb from some regions, such that it can accumulate at others, it implies that there must be insufficient polycomb to both accumulate across the genome when BAF is depleted and maintain repression. To test this, we wanted a system where we can rapidly degrade PRCs in a dose-dependent way and measure the degree of gene derepression relative to Brg1 at the same time-point. For this goal, we used the dTAG targeted degradation approach, which enables highly dose-dependent, specific, and efficient protein degradation (Nabet et al., 2018). We tagged endogenous alleles of essential subunits of PRC1 (Ring1b), PRC2 (EED), and both proteins in the same cell line with the $FKBP^{F36V}$ tag that enables targeted degradation in the presence of dTAG13, an heterobifunctional analog of rapamycin (Stanton et al., 2018). EED, is required to maintain global levels of H3K27me3 and to stabilize other subunits of the PRC2 complex (Montgomery et al., 2005). Tagging these proteins didn't noticeably affect protein abundance, cell viability, or growth (Figure 6A,B,

Supplementary Figure 6A, B).

We observed step-wise near complete degradation of EED using 10-fold serial dilution of dTAG13 ligand at 8h (Figure 6C) (maximal degradation is achieved by 2h similar to Brg1). We then asked if genes derepressed by Brg1 degradation, including 11 Hox genes across three clusters (A, B, and D) and a few canonical highly polycomb-bound genes (Bmi1, Meis2, and Pax6) are sensitive to PRC2 dosage. Surprisingly, we found that even maximal degradation was not sufficient to derepress any of the genes assayed. So, we next tested Ring1b, which could also be degraded in a dose-dependent manner similar to EED (Figure 6D). Yet, unlike the EED degron, most of these genes became derepressed by Ring1b degradation in a dose-dependent manner (Figure 6D). Many genes phenocopied the Brg1 degron effect at intermediate levels of degradation and derepressed more at maximal near-complete depletion (Figure 6D bottom and 6F). However, a few genes still exhibited stronger derepression in the Brg1 degron than Ring1b, even upon near-complete Ring1b degradation (Figure 6D, bottom). Our previous ChIP-seq experiments revealed that Brg1 degradation results in the redistribution of both PRC1&2, so we next sought to determine the effect of depleting both subunits in the same cell (Figure 6E). We found that indeed, there was an additive effect of degrading Ring1b and EED on derepression, with all genes exhibiting similar derepression as Brg1 at intermediate levels, and either stronger or the same level upon maximal degradation (Figure 6E, bottom). These results demonstrate that complete loss of PRC1&2 leads to stronger derepression than Brg1, however intermediate loss closely resembles the

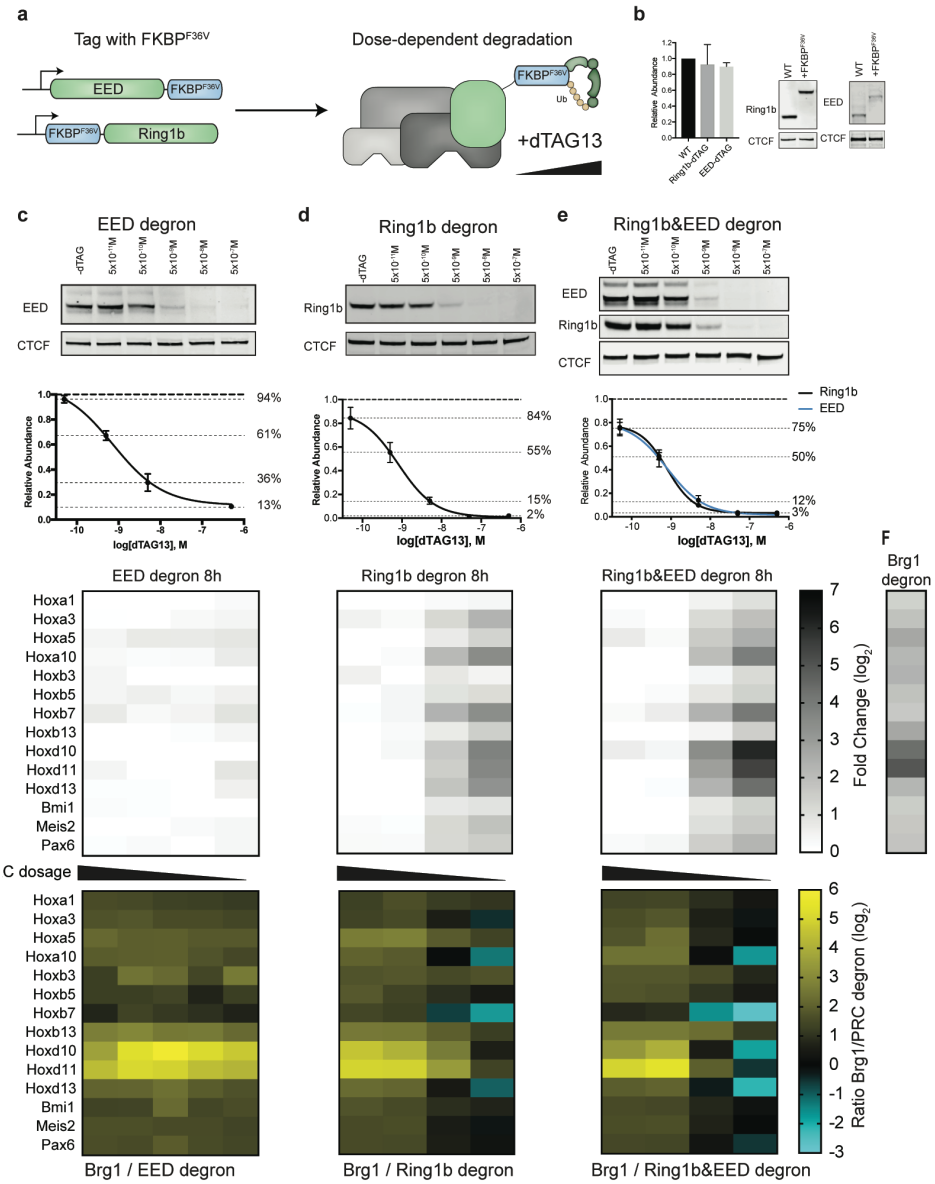

Figure 6: PRC1&2 dosage sensitivity underlies the requirement for BAF in repression
(a) Schematic depicting EED and Ring1b dTAG targeted protein degradation strategy in mESCs, where EED is tagged at the C-terminus and Ring1b is tagged at the N-terminus. (b) Representative western blot and quantitation of EED and Ring1b abundance in parent line compared to lines tagged with FKBP^{F36V}. Error bars depict mean +/- standard error of the mean from three tagged EED lines and four tagged Ring1b lines. (c) Representative western and quantification for 10-fold dilution of dTAG13 PROTAC of Ring1b. Error bars depict mean +/- standard error of the mean from four different cell lines. (d) qRT-PCR at four different dTAG doses indicated in (c) and the ratio of Brg1 degron / Ring1b-degron (Log_2-transformed) at different doses (bottom). (e,f) Ring1b&EED-dTAG degradation dose response and qRT-PCR, similar to (c,d). Error bars depict mean +/- standard error of the mean from four different cell lines. (g) Fold change (Log_2-transformed) on derepression in Brg1 degron for comparison. All experiments were conducted at 8h degradation.

343 derepressive effect of Brg1 degradation. Thus, by directly targeting both sides of the BAF-PRC axis we
344 reveal that dosage-sensitivity underlies the mechanism by which BAF facilitates polycomb-mediated
345 repression.

346

347 **Increased PRC1 dosage inhibits Brg1 degron mediated derepression**

348 We reasoned that if we conduct the opposite of our PRC1&2 degron experiments and overexpress
349 polycomb, then the increased dosage should be sufficient to both redistribute but also maintain repression
350 of Hox genes when Brg1 is degraded. This is inherently challenging considering that there are numerous
351 different PRC1 and PRC2 subunits that are expressed in ESCs, each with their own contribution to
352 repression. Yet, our degradation experiments showed a more prominent role for PRC1 over PRC2 in
353 repressing Hox genes. While canonical PRC1 does have a role in Hox gene repression (Kundu et al.,
354 2018), the catalytic activity of PRC1 is most essential for transcriptional repression in ESCs (Blackledge
355 et al., 2019; Tamburri et al., 2019), where the H2AK119ub1 mark is predominately placed by the more
356 catalytically active variant PRC1 (vPRC1) (Fursova et al., 2019; Gao et al., 2012; Morey et al., 2013;
357 Rose et al., 2016). So, we next sought to overexpress in our Brg1 degron cells, a minimal vPRC1 complex
358 containing Ring1b and PCGF1, which stabilize each other (Ben-Saadon et al., 2006). Despite expression
359 with a strong EF1a promoter, we obtained modest ~2x increase in H2AK119ub1 levels over vector only
360 control with this minimal complex (Figure 7a). Next we conducted a series of 8h Brg1 degron experiments
361 to compare the magnitude of derepression. We obtained similar Brg1 degradation efficiencies between
362 vector and vPRC1 overexpression cells (95+/-3.5 and 91+/-3.0 percent degraded respectively) but
363 observed consistently less derepression in cells overexpressing the minimal vPRC1 compared to empty
364 vector for all genes tested (Figure 7B). Thus, increased dosage of just a minimal variant PRC1 complex
365 is sufficient to inhibit Brg1 degron mediated derepression, further supporting our model that BAF
366 generates polycomb dosage that is needed for repression.

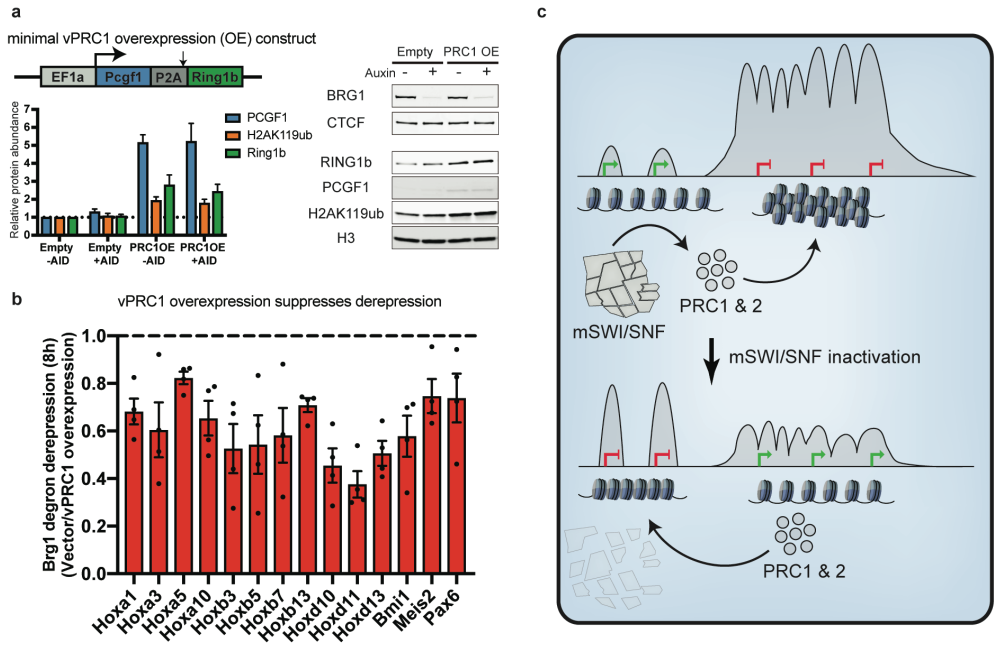

Figure 7: Increased PRC1 dosage inhibits Brg1 degron mediated derepression
(a) (left) Western blot quantification of PCGF1, H2AK119ub, and Ring1b relative to vector only -AID control cells. (right) representative western blot showing Brg1 degron and minimal vPRC1 overexpression (b) Ratio of ddCt values for vector / vPRC1 overexpression. n = 4 biological replicates. Error bars represent S.E.M. (c) Model. mSWI/SNF opposes PRC1 complexes across the genome, which enable accumulation at heavily occupied sites like Hox, facilitating the repression of these genes. When mSWI/SNF is inactivated, PRC complexes accumulate where mSWI/SNF normally evicts them causing the redistribution away from heavily occupied sites leading to derepression.

367

368

369 **Discussion**

370 Our studies demonstrate that targeted degradation of Brg1, the ATPase subunit of the BAF complex,
371 rapidly derepressed hundreds of strongly polycomb-repressed genes on the timescale of hours.

372 Surprisingly, we found that derepression was caused by rapid genome-wide redistribution of both PRC1
373 and PRC2 complexes from highly occupied domains where BAF is mostly excluded, to lowly bound loci
374 that are targeted by both BAF and polycomb. The redistribution of polycomb led to the physical
375 decompaction of repressed Hox clusters and opposite changes to chromatin features associated with active
376 transcription. These results led us to propose that limiting polycomb dosage in mESCs underlies these
377 effects, such that BAF-mediated displacement at many weakly bound sites controls the dosage of
378 polycomb and extent of repression at distal sites (Figure 7c). We provide extensive support for this model
379 both by temporally titrating PRC1&2 dosage and defining the extent of derepression and by showing that
380 PRC1 overexpression inhibits Brg1 degron mediated derepression. Thus, by antagonizing polycomb
381 across the genome, BAF titrates polycomb dosage to promote distal repression.
382
383 These data resolve long-standing questions in the field regarding the BAF-polycomb axis in gene
384 regulation. Extensive studies have shown that SWI/SNF has a direct and conserved role in antagonizing
385 polycomb to promote gene activation (Bracken et al., 2019). Yet, paradoxically, BAF was also shown to
386 function in the reverse direction to promote polycomb-mediated repression (Alexander et al., 2015; Ho et
387 al., 2011; Johann et al., 2016). A mechanism to explain how BAF both places and displaces polycomb-
388 repressive complexes is currently lacking. For example, homologous complexes in Drosophila are
389 activators of Hox genes (Tamkun et al., 1992), not repressors, and direct chemically induced BAF
390 recruitment in mammalian cells only led to polycomb eviction (Braun et al., 2017; Kadoch et al., 2017;
391 Stanton et al., 2017), calling into question whether BAF directly promotes polycomb-mediated repression
392 and how?

393 A primary limitation to addressing this paradox, and many others across the biological sciences, has been
394 the inability to assay loss of function at sufficiently short timescales to rule out far downstream secondary
395 effects. While, inhibitory small molecules are best for this goal, due to their speed of action and
396 reversibility, the vast majority of the proteome remains untargetable (Wishart et al., 2018). Widely used
397 depletion approaches such as RNAi or conditional knockouts are useful, but these approaches target RNA
398 and operate on the timescale of days. Indeed, many of the genes thought to be regulated by BAF from
399 conditional inactivation are likely to reflect cell cycle exit and cell death. By leveraging new chemical
400 induced proximity approaches that rapidly and efficiently degrade proteins (Stanton et al., 2018), we are
401 able to define the timescale by which BAF promotes polycomb-mediated repression lacking in other
402 studies (Alexander et al., 2015; Ho et al., 2011). Targeted degradation enabled us to conclude that BAF
403 driven polycomb redistribution happens on timescales inconsistent with secondary effects caused by
404 deregulation of a few genes, or cell death. Surprisingly, the magnitude of the transcriptional derepression
405 we observe is much stronger (up to ~40x higher) than was previously observed with conditional
406 knockouts, demonstrating that rapid degradation approaches are also less subject to secondary feedback
407 mechanisms.

408 Polycomb-mediated repression has long been known to be dosage sensitive, such that heterozygous
409 genetic deletion alters expression of Hox genes, giving rise to homeotic transformations (Kennison and
410 Tamkun, 1988). Intriguingly, most PRC genes themselves don't appear to be strongly dosage-sensitive in
411 human disease (Karczewski et al., 2019). An interesting conclusion from our work is that chromatin
412 regulators that antagonize binding, like BAF and possibly others, titrate the effective dosage of all
413 Polycomb complexes and could explain why many BAF subunits are strongly haploinsufficient in human
414 disease. Previously it was shown that PRC1 eviction by BAF was mediated by a direct ATP-dependent
415 interaction with Brg1 (Stanton et al., 2017). Future studies are needed to define the role of other subunits
416 in polycomb antagonism. Nonetheless, our studies suggest that BAF activity is a major determinant of
417 polycomb dynamics in ES cells, which have a hypermobile polycomb fraction (Fonseca et al., 2012).
418 Thus, it's possible that this dynamic state is especially sensitive to modulation on chromatin, as BAF has

419 been shown to facilitate polycomb-mediated repression in pluripotency, during lineage commitment, and
420 in pediatric brain tumors but not in more differentiated cells.

421 While individual BAF subunits are highly mutated in specific types of cancer, BAF is almost exclusively
422 mutated in neurodevelopmental disorders but not in other types of human disease (Kadoch and Crabtree,
423 2015). The underlying mechanism for this specificity remains unknown. Our results suggest an
424 explanation by which BAF's unique ability to modulate effective polycomb dosage on chromatin in
425 pluripotent cells that, in turn, leads to derepression of genes involved in neurogenesis. A possible
426 explanation for this specificity arises from the observation that the mRNA for certain posterior Hox genes
427 such as Hoxd10 increase by 400-fold upon BAF degradation. This would cause the embryo with a
428 mutation in the BAF complex to enter neurogenesis with posterior hox genes expressed in developing
429 neural tissue. Based on murine studies this "hox confusion" would lead to temporally disordered patterns
430 of gene expression in neural progenitors and abnormal neural development (Philippidou and Dasen, 2013).
431 Consistent with this, Brg1 knockdown in blastocysts leads to aberrant Hox gene derepression (Kidder et
432 al., 2009). While proper examination of this hypothesis would require complex genetic models, it provides
433 a potential explanation for the surprising neural specificity of BAF subunit mutations.

434 **Methods**

435 **Mouse ESC culture**

436 TC1(129) mouse embryonic stem cells were cultured in Knockout™ Dulbeecco's Modified Eagle's
437 Medium (Thermo Fisher #10829018) supplemented with 7.5% ES-qualified serum (Applied Stem Cell
438 #ASM-5017), 7.5% Knockout™ Serum replacement (Thermo Fisher #10828-028), 2mM L-glutamine
439 (Gibco #35050061), 10mM HEPES (Gibco #15630080), 100 units mL^{-1} penicillin/streptomycin (Gibco
440 #151401222), 0.1mM non-essential amino acids (Gibco #11140050), 0.1mM beta-mercaptoethanol
441 (Gibco #21985023), and LIF. ES cells were maintained on gamma-irradiated mouse embryonic fibroblast
442 (MEF) feeders for passage or gelatin-coated dishes for assays at 37ºC with 5% CO_2, seeded at
443 ~$3.6x10^4/cm^2$ every 48 hours, with daily media changes. For 2i experiments, cells were transitioned to 2i
444 media (Ying et al., 2008) for 4 passages prior to conducting assays. To degrade Brg1, osTIR1 was induced
445 overnight with 1.0 µg/mL doxycycline and media containing 0.5 µM 3-indoleacetic acid (Sigma # I2886)
446 and doxycycline was added for indicated time-points. To degrade EED and Ring1b, dTAG-13 was added
447 for indicated time and concentration (from $5x10^{-7}$-$5x10^{-11}$M). All lines tested negative for mycoplasma.
448

449 **CRISPR/Cas9 genome editing**

450 Low passage TC1(129) mouse embryonic stem cells were thawed onto MEF coated dishes and passaged
451 once on gelatin coated dishes before transfection. 2M cells were nucleofected (Lonza #VVPH-1001, A-
452 013 program) with 8µg HDR template and 4µg PX459V2.0 (Addgene #62988) containing single guide
453 RNAs (below) or 2µM RNP (IDT #1081058) for dTAG-Ring1b. HDR templates contained 0.5 or 1kB
454 homology arms flanking AID* or $FKBP^{F36V}$ degradation and epitope tags, which were inserted with a
455 flexible $(GGGGS)_3$ linker between endogenous protein and the tags. Brg1 and EED were tagged at the C-
456 terminus and Ring1b was tagged at the N-terminus. Following transfection 0.5M cells were seeded onto
457 6cm dishes coated with DR4 MEFS and cultured for 24 hours before puromycin selection (1.0 µg/mL,
458 1.25 µg/mL, or 1.5 µg/mL) for 48 hours or $1x10^{3-5}$ cells without selection for RNP. Single colonies were
459 manually picked, dissociated with trypsin and expanded on MEFs. Colonies containing homozygous
460 insertions were confirmed by PCR and western blotting. Guide sequences are as follows: Brg1 sgRNA:
461 TTGGCTGGGACGAGCGCCTC, EED sgRNA: TGATGCCAGCATTTGGCGAT, Ring1b sgRNA:
462 TTTATTCCTAGAAATGTCTC.
463

464 **Lentiviral preparation and delivery**

465 HEK293T cells were transfected with gene delivery constructs and packaging plasmids Md2G and
466 psPAX2 using polyethylenimine (PEI). Two days post transfection the media was collected,
467 filtered, and centrifuged at 50,000 × *g* for 2 hours at 4 °C. The concentrated viral pellet was
468 resuspended in PBS and used directly for transduction or frozen at -80ºC. Lentivirus encoding
469 rtTA and TRE-osTIR1 were added to low-passage Brg1-AID* edited cells and selected with 1µg mL^{-1}
470 puromycin and 100µg mL^{-1} hygromycin B.
471
472 **RNA isolation and qRT-PCR**
473 Cells were dissociated with trypsin, quenched with media, washed with PBS, and immediately
474 resuspended in Trisure (Bioline # BIO-38033). Total RNA was isolated following manufacturer's
475 guidelines, digested with DNaseI (Thermo Fischer #18068015), and digestion reaction was cleaned up
476 with acid-phenol:chloroform. cDNA was synthesized from 1µg RNA using the sensifast kit (Bioline
477 #BIO-65054). Primer sequences are in (Supplemental Table 1) and was normalized to GAPDH using the
478 ΔΔCt method.
479
480 **RNA-seq and data analysis**
481 RNA sequencing libraries were made from 1µg RNA (RIN > 9) using the SMARTer kit (Takara Bio #
482 634874) which produces stranded libraries from rRNA depleted total RNA. Libraries were amplified with
483 12 PCR cycles, quantified with Qubit, and size distribution was determined by Bioanalyzer. Libraries
484 were sequenced single-end with 76 cycles on an Illumina Nextseq and the first three bases were trimmed
485 with cutadapt (Martin) before quantification. Transcript abundances were quantified by Kallisto (Bray et
486 al., 2016)using the UCSC transcript tables for the mm10 genome assembly. Transcript-level abundance
487 estimates from Kallisto and gene-level count matrices were created using Tximport (Soneson et al., 2015).
488 Differential expression analysis was conducted with DESeq2 version 1.22.2 (Love et al., 2014) using
489 default parameters, after prefiltering genes with low counts (rowSums > 10). Differential calls were made
490 by requiring FDR-corrected $P < 0.05$. Genome browser tracks were generated by aligning trimmed reads
491 to the mm10 genome with HISAT2 (Kim et al., 2015) with appropriate RNA-strandedness option and
492 deepTools (Ramirez et al., 2016) was used to generate read depth normalized bigwig files, scaled to the
493 mouse genome size (RPGC), for viewing with IGV (Robinson et al., 2011). Gene ontology analysis was
494 conducted with DAVID (Huang da et al., 2009).
495
496 **ChIP and ChIP-qPCR**
497 ChIP experiments were performed essentially as described (Braun et al., 2017). Briefly, at the end of the
498 time-point 30M cells were fixed with 1% formaldehyde for 12 min, quenched, and sonicated with a
499 Covaris focused ultrasonicator (~200-800bp). Sonicated chromatin was split into separate tubes (~5-10M
500 cell equivalent per IP) and incubated with 5µg primary antibody and 25µL protein G Dynabeads (Life
501 Technologies 10009D) overnight. Beads were washed 4 times and DNA was isolated for qPCR or library
502 preparation. Antibodies are listed in supplemental Table 2. Primer sequences for qPCR experiments are
503 in Supplemental table 1.
504
505 **ChIP-seq and data analysis**
506 ChIP-seq libraries were made using NEBnext Ultra II (NEB E7013) with ≤ 12 PCR cycles. Libraries were
507 quantified with Qubit, and size distribution was determined by Bioanalyzer. Libraries were sequenced
508 single-end with 76 cycles on an Illumina Nextseq. Reads were aligned to the mm10 genome with Bowtie
509 2 (Langmead and Salzberg, 2012)version 2.3.4.1 with the --very-sensitive option. Alignments were
510 removed with the following criteria: quality score < 20, PCR duplicates, secondary alignments, and
511 supplemental alignments. Peaks were called with MACS2 using default parameters and requiring that q <
512 0.01. Peaks from control and treated datasets within +/- 1kb were merged, filtered against the mouse
513 blacklist (Amemiya et al., 2019) and the number of reads overlapping these peak sets were compared for

514 differential peak calling. Differential peak calls were determined using DESeq2 after pre-filtering peaks
515 with low counts (rowSums > 400 for Ring1b & Suz12 with four biological replicates, and rowSums > 100
516 for histone marks with two biological replicates. Differential calls were made by requiring FDR-corrected
517 $P < 0.1$. Read depth normalized genome coverage files (bigwig) were generated with deepTools (Ramirez
518 et al., 2016), scaled to the mouse genome size (RPGC). Replicate BAM files were merged and bigwig
519 files were normalized before subtraction (8 hour – 0 hour) for visualization by heatmap, metagene plot, or
520 by browser (IGV).
521
522 **RNA polymerase inhibition**
523 Transcription initiation was blocked by treating cells with 10 μM triptolide (Sellec S3604). To validate
524 triptolide treatment, quantitative RT-PCR was performed by comparing derepressed genes in triptolide,
525 triptolide and IAA, to IAA only cells, normalized to U6 snRNA using the ΔΔCt method.
526
527 **ORCA Imaging and data analysis**
528 The primary probes tiling the HoxA and HoxD DNA regions at 5kb resolution (Supplemental data), were
529 designed as previously described (Mateo et al., 2019). Probes were amplified from the oligopool
530 (CustomArray), and amplified according to the protocol described in (Boettiger et al., 2016; Mateo et al.,
531 2019).
532
533 In preparation for imaging, mESC cells were plated on 40-mm glass coverslips (Bioptechs) coated with
534 0.1-0.2% Gelatin, and fixed on the following day in 4% PFA in 1xPBS for 10 min. The hybridization and
535 imaging were performed as previously described (Mateo et al. 2019). Briefly, for primary probe
536 hybridization, cells were permeabilized for 10min with 0.5% Triton-X in 1xPBS, the DNA was then
537 denatured by treatment with 0.1M HCL for 5min. 2ug of primary probes in hybridization solution was
538 then added directly on to cells, placed on a heat block for 90C for 3min and incubated overnight at 42C in
539 a humidified chamber. Prior to imaging, the samples were post-fixed for 1h in 8%PFA +2%
540 glutaraldehyde (GA) in 1xPBS. The samples were then washed in 2xSSC and either imaged directly or
541 stored for up to a week in 4C prior to imaging. For imaging samples were mounted into a Bioptechs flow
542 chamber, and secondary probe hybridization and step by step imaging of individual barcodes, and image
543 processing was performed as in (Mateo et al., 2019).
544
545 Image analysis was performed as described in (Mateo et al., 2019). For all analysis in Figure 4, we
546 excluded all barcodes that had a low labeling efficiency in either control or AID treated condition (labelled
547 in less than 10% of the cells). This resulted in a final of 52 barcodes for HoxA and 28 barcodes for HoxD.
548 For comparison with HiC, mESC data from (Bonev et al., 2017) was downloaded from Juicebox (Durand
549 et al., 2016; Robinson et al., 2018) and matched to ORCA barcode coordinates by finding the closest
550 genomic bins in HiC, and removing bins corresponding to excluded barcodes. ORCA data was processed
551 to calculate contact frequency across all cells (Supplemental Figure 4 A, B), where contact frequency was
552 computed by calculating the fraction of cells where the probes were within a 200 nm distance. We use
553 'cell' to refer to all detected spots, with ~2 spots per cell, corresponding to each allele. For calculation of
554 median probe distance (to generate Figures 4E, F) we calculated the median distance across all cells in
555 each condition. For both HoxA and HoxD imaging, we obtained more cells in the control condition (1238
556 for HoxA, 2419 for HoxD) than in the AID treated condition (587 for HoxA and 1183 for HoxD). To
557 control for sample size, we randomly split the cells in the control dataset into 2, calculated median of
558 pairwise probe distances for each subset and computed the difference in pairwise distances between the
559 two halves and between each control subset and Brg1 depleted cells (Supplemental Figure 4D, E).
560
561 **Data availability**
562 All sequencing data have been deposited in GEO (accession number XXXXXXX)

Acknowledgements

We thank members of the Crabtree lab for insightful comments and discussions over the course of the study. We are grateful to Srinivas Ramachandran (CU Anschutz) and Vijay Ramani (UCSF) for providing critical comments on the manuscript and for helpful discussions. This study was supported by NIH grants R01CA163915 (G.R.C), R37NS046789 (G.R.C), DP2GM132935 (A.N.B.), the Howard Hughes Medical Institute (G.R.C), Swiss National Science Foundation (SNSF) postdoctoral fellowship (S.M.G.B.), the Walter V. and Idun Berry Postdoctoral fellowship program (C.M.W. and T.A.), and the Sir James Black postdoctoral fellowship (C.M.W. and S.M.G.B.).

Author Contributions

C.M.W conceived of the project, did experiments, and analysis. T.A. performed ORCA experiments and analysis. S.M.G.B. performed experiments. G.R.C and A.N.B. designed experiments and supervised the project. C.M.W wrote the paper with assistance from all authors.

References

Alexander, J.M., Hota, S.K., He, D., Thomas, S., Ho, L., Pennacchio, L.A., and Bruneau, B.G. (2015). Brg1 modulates enhancer activation in mesoderm lineage commitment. Development *142*, 1418-1430.

Amemiya, H.M., Kundaje, A., and Boyle, A.P. (2019). The ENCODE Blacklist: Identification of Problematic Regions of the Genome. Sci Rep *9*, 9354.

Ben-Saadon, R., Zaaroor, D., Ziv, T., and Ciechanover, A. (2006). The polycomb protein Ring1B generates self atypical mixed ubiquitin chains required for its in vitro histone H2A ligase activity. Mol Cell *24*, 701-711.

Bensaude, O. (2011). Inhibiting eukaryotic transcription: Which compound to choose? How to evaluate its activity? Transcription *2*, 103-108.

Bintu, B., Mateo, L.J., Su, J.H., Sinnott-Armstrong, N.A., Parker, M., Kinrot, S., Yamaya, K., Boettiger, A.N., and Zhuang, X. (2018). Super-resolution chromatin tracing reveals domains and cooperative interactions in single cells. Science *362*.

Blackledge, N.P., Fursova, N.A., Kelley, J.R., Huseyin, M.K., Feldmann, A., and Klose, R.J. (2019). PRC1 Catalytic Activity Is Central to Polycomb System Function. Mol Cell.

Boettiger, A.N., Bintu, B., Moffitt, J.R., Wang, S., Beliveau, B.J., Fudenberg, G., Imakaev, M., Mirny, L.A., Wu, C.T., and Zhuang, X. (2016). Super-resolution imaging reveals distinct chromatin folding for different epigenetic states. Nature *529*, 418-422.

Bonev, B., Mendelson Cohen, N., Szabo, Q., Fritsch, L., Papadopoulos, G.L., Lubling, Y., Xu, X., Lv, X., Hugnot, J.P., Tanay, A.*, et al.* (2017). Multiscale 3D Genome Rewiring during Mouse Neural Development. Cell *171*, 557-572 e524.

Boyer, L.A., Plath, K., Zeitlinger, J., Brambrink, T., Medeiros, L.A., Lee, T.I., Levine, S.S., Wernig, M., Tajonar, A., Ray, M.K.*, et al.* (2006). Polycomb complexes repress developmental regulators in murine embryonic stem cells. Nature *441*, 349-353.

603 Bracken, A.P., Brien, G.L., and Verrijzer, C.P. (2019). Dangerous liaisons: interplay between SWI/SNF,
604 NuRD, and Polycomb in chromatin regulation and cancer. Genes Dev *33*, 936-959.

605 Braun, S.M.G., Kirkland, J.G., Chory, E.J., Husmann, D., Calarco, J.P., and Crabtree, G.R. (2017).
606 Rapid and reversible epigenome editing by endogenous chromatin regulators. Nat Commun *8*, 560.

607 Bray, N.L., Pimentel, H., Melsted, P., and Pachter, L. (2016). Near-optimal probabilistic RNA-seq
608 quantification. Nat Biotechnol *34*, 525-527.

609 Clapier, C.R., Iwasa, J., Cairns, B.R., and Peterson, C.L. (2017). Mechanisms of action and regulation of
610 ATP-dependent chromatin-remodelling complexes. Nat Rev Mol Cell Biol *18*, 407-422.

611 Durand, N.C., Shamim, M.S., Machol, I., Rao, S.S., Huntley, M.H., Lander, E.S., and Aiden, E.L.
612 (2016). Juicer Provides a One-Click System for Analyzing Loop-Resolution Hi-C Experiments. Cell
613 Syst *3*, 95-98.

614 Ernst, J., and Kellis, M. (2012). ChromHMM: automating chromatin-state discovery and
615 characterization. Nat Methods *9*, 215-216.

616 Eskeland, R., Leeb, M., Grimes, G.R., Kress, C., Boyle, S., Sproul, D., Gilbert, N., Fan, Y., Skoultchi,
617 A.I., Wutz, A.*, et al.* (2010). Ring1B compacts chromatin structure and represses gene expression
618 independent of histone ubiquitination. Mol Cell *38*, 452-464.

619 Flavahan, W.A., Gaskell, E., and Bernstein, B.E. (2017). Epigenetic plasticity and the hallmarks of
620 cancer. Science *357*.

621 Fonseca, J.P., Steffen, P.A., Muller, S., Lu, J., Sawicka, A., Seiser, C., and Ringrose, L. (2012). In vivo
622 Polycomb kinetics and mitotic chromatin binding distinguish stem cells from differentiated cells. Genes
623 Dev *26*, 857-871.

624 Francis, N.J., Kingston, R.E., and Woodcock, C.L. (2004). Chromatin compaction by a polycomb group
625 protein complex. Science *306*, 1574-1577.

626 Fursova, N.A., Blackledge, N.P., Nakayama, M., Ito, S., Koseki, Y., Farcas, A.M., King, H.W., Koseki,
627 H., and Klose, R.J. (2019). Synergy between Variant PRC1 Complexes Defines Polycomb-Mediated
628 Gene Repression. Mol Cell *74*, 1020-1036 e1028.

629 Gao, Z., Zhang, J., Bonasio, R., Strino, F., Sawai, A., Parisi, F., Kluger, Y., and Reinberg, D. (2012).
630 PCGF homologs, CBX proteins, and RYBP define functionally distinct PRC1 family complexes. Mol
631 Cell *45*, 344-356.

632 Gatchalian, J., Malik, S., Ho, J., Lee, D.S., Kelso, T.W.R., Shokhirev, M.N., Dixon, J.R., and
633 Hargreaves, D.C. (2018). A non-canonical BRD9-containing BAF chromatin remodeling complex
634 regulates naive pluripotency in mouse embryonic stem cells. Nat Commun *9*, 5139.

635 Hainer, S.J., Gu, W., Carone, B.R., Landry, B.D., Rando, O.J., Mello, C.C., and Fazzio, T.G. (2015).
636 Suppression of pervasive noncoding transcription in embryonic stem cells by esBAF. Genes Dev *29*,
637 362-378.

638 Ho, L., Jothi, R., Ronan, J.L., Cui, K., Zhao, K., and Crabtree, G.R. (2009). An embryonic stem cell
639 chromatin remodeling complex, esBAF, is an essential component of the core pluripotency
640 transcriptional network. Proc Natl Acad Sci U S A *106*, 5187-5191.

641 Ho, L., Miller, E.L., Ronan, J.L., Ho, W.Q., Jothi, R., and Crabtree, G.R. (2011). esBAF facilitates
642 pluripotency by conditioning the genome for LIF/STAT3 signalling and by regulating polycomb
643 function. Nat Cell Biol *13*, 903-913.

644 Hodges, H.C., Stanton, B.Z., Cermakova, K., Chang, C.Y., Miller, E.L., Kirkland, J.G., Ku, W.L.,
645 Veverka, V., Zhao, K., and Crabtree, G.R. (2018). Dominant-negative SMARCA4 mutants alter the
646 accessibility landscape of tissue-unrestricted enhancers. Nat Struct Mol Biol *25*, 61-72.

647 Huang da, W., Sherman, B.T., and Lempicki, R.A. (2009). Bioinformatics enrichment tools: paths
648 toward the comprehensive functional analysis of large gene lists. Nucleic Acids Res *37*, 1-13.

649 Johann, P.D., Erkek, S., Zapatka, M., Kerl, K., Buchhalter, I., Hovestadt, V., Jones, D.T.W., Sturm, D.,
650 Hermann, C., Segura Wang, M.*, et al.* (2016). Atypical Teratoid/Rhabdoid Tumors Are Comprised of
651 Three Epigenetic Subgroups with Distinct Enhancer Landscapes. Cancer Cell *29*, 379-393.

652 Joshi, O., Wang, S.Y., Kuznetsova, T., Atlasi, Y., Peng, T., Fabre, P.J., Habibi, E., Shaik, J., Saeed, S.,
653 Handoko, L.*, et al.* (2015). Dynamic Reorganization of Extremely Long-Range Promoter-Promoter
654 Interactions between Two States of Pluripotency. Cell Stem Cell *17*, 748-757.

655 Kadoch, C., and Crabtree, G.R. (2013). Reversible disruption of mSWI/SNF (BAF) complexes by the
656 SS18-SSX oncogenic fusion in synovial sarcoma. Cell *153*, 71-85.

657 Kadoch, C., and Crabtree, G.R. (2015). Mammalian SWI/SNF chromatin remodeling complexes and
658 cancer: Mechanistic insights gained from human genomics. Sci Adv *1*, e1500447.

659 Kadoch, C., Williams, R.T., Calarco, J.P., Miller, E.L., Weber, C.M., Braun, S.M., Pulice, J.L., Chory,
660 E.J., and Crabtree, G.R. (2017). Dynamics of BAF-Polycomb complex opposition on heterochromatin in
661 normal and oncogenic states. Nat Genet *49*, 213-222.

662 Karczewski, K.J., Francioli, L.C., Tiao, G., Cummings, B.B., Alföldi, J., Wang, Q., Collins, R.L.,
663 Laricchia, K.M., Ganna, A., Birnbaum, D.P.*, et al.* (2019). Variation across 141,456 human exomes and
664 genomes reveals the spectrum of loss-of-function intolerance across human protein-coding genes.
665 bioRxiv.

666 Kennison, J.A., and Tamkun, J.W. (1988). Dosage-dependent modifiers of polycomb and antennapedia
667 mutations in Drosophila. Proc Natl Acad Sci U S A *85*, 8136-8140.

668 Kidder, B.L., Palmer, S., and Knott, J.G. (2009). SWI/SNF-Brg1 regulates self-renewal and occupies
669 core pluripotency-related genes in embryonic stem cells. Stem Cells *27*, 317-328.

670 Kim, D., Langmead, B., and Salzberg, S.L. (2015). HISAT: a fast spliced aligner with low memory
671 requirements. Nat Methods *12*, 357-360.

672 King, H.W., Fursova, N.A., Blackledge, N.P., and Klose, R.J. (2018). Polycomb repressive complex 1
673 shapes the nucleosome landscape but not accessibility at target genes. Genome Res *28*, 1494-1507.

674 Kingston, R.E., and Tamkun, J.W. (2014). Transcriptional regulation by trithorax-group proteins. Cold
675 Spring Harb Perspect Biol *6*, a019349.

676 Kundu, S., Ji, F., Sunwoo, H., Jain, G., Lee, J.T., Sadreyev, R.I., Dekker, J., and Kingston, R.E. (2018).
677 Polycomb Repressive Complex 1 Generates Discrete Compacted Domains that Change during
678 Differentiation. Mol Cell *71*, 191.

679 Langmead, B., and Salzberg, S.L. (2012). Fast gapped-read alignment with Bowtie 2. Nat Methods *9*,
680 357-359.

681 Love, M.I., Huber, W., and Anders, S. (2014). Moderated estimation of fold change and dispersion for
682 RNA-seq data with DESeq2. Genome Biol *15*, 550.

683 Martin, M. Cutadapt Removes Adapter Sequences From High-Throughput Sequencing Reads.

684 Masliah-Planchon, J., Bieche, I., Guinebretiere, J.M., Bourdeaut, F., and Delattre, O. (2015). SWI/SNF
685 chromatin remodeling and human malignancies. Annu Rev Pathol *10*, 145-171.

686 Mateo, L.J., Murphy, S.E., Hafner, A., Cinquini, I.S., Walker, C.A., and Boettiger, A.N. (2019).
687 Visualizing DNA folding and RNA in embryos at single-cell resolution. Nature *568*, 49-54.

688 McBride, M.J., Pulice, J.L., Beird, H.C., Ingram, D.R., D'Avino, A.R., Shern, J.F., Charville, G.W.,
689 Hornick, J.L., Nakayama, R.T., Garcia-Rivera, E.M.*, et al.* (2018). The SS18-SSX Fusion Oncoprotein
690 Hijacks BAF Complex Targeting and Function to Drive Synovial Sarcoma. Cancer Cell *33*, 1128-1141
691 e1127.

692 Miller, E.L., Hargreaves, D.C., Kadoch, C., Chang, C.Y., Calarco, J.P., Hodges, C., Buenrostro, J.D.,
693 Cui, K., Greenleaf, W.J., Zhao, K.*, et al.* (2017). TOP2 synergizes with BAF chromatin remodeling for
694 both resolution and formation of facultative heterochromatin. Nat Struct Mol Biol *24*, 344-352.

695 Montgomery, N.D., Yee, D., Chen, A., Kalantry, S., Chamberlain, S.J., Otte, A.P., and Magnuson, T.
696 (2005). The murine polycomb group protein Eed is required for global histone H3 lysine-27
697 methylation. Current Biology *15*, 942-947.

698 Morawska, M., and Ulrich, H.D. (2013). An expanded tool kit for the auxin-inducible degron system in
699 budding yeast. Yeast *30*, 341-351.

700 Morey, L., Aloia, L., Cozzuto, L., Benitah, S.A., and Di Croce, L. (2013). RYBP and Cbx7 define
701 specific biological functions of polycomb complexes in mouse embryonic stem cells. Cell Rep *3*, 60-69.

702 Nabet, B., Roberts, J.M., Buckley, D.L., Paulk, J., Dastjerdi, S., Yang, A., Leggett, A.L., Erb, M.A.,
703 Lawlor, M.A., Souza, A.*, et al.* (2018). The dTAG system for immediate and target-specific protein
704 degradation. Nat Chem Biol *14*, 431-441.

705 Nakayama, R.T., Pulice, J.L., Valencia, A.M., McBride, M.J., McKenzie, Z.M., Gillespie, M.A., Ku,
706 W.L., Teng, M., Cui, K., Williams, R.T.*, et al.* (2017). SMARCB1 is required for widespread BAF
707 complex-mediated activation of enhancers and bivalent promoters. Nat Genet *49*, 1613-1623.

708 Nishimura, K., Fukagawa, T., Takisawa, H., Kakimoto, T., and Kanemaki, M. (2009). An auxin-based
709 degron system for the rapid depletion of proteins in nonplant cells. Nat Methods *6*, 917-922.

710 Nora, E.P., Goloborodko, A., Valton, A.L., Gibcus, J.H., Uebersohn, A., Abdennur, N., Dekker, J.,
711 Mirny, L.A., and Bruneau, B.G. (2017). Targeted Degradation of CTCF Decouples Local Insulation of
712 Chromosome Domains from Genomic Compartmentalization. Cell *169*, 930-944 e922.

713 Philippidou, P., and Dasen, J.S. (2013). Hox genes: choreographers in neural development, architects of
714 circuit organization. Neuron *80*, 12-34.

715 Piunti, A., and Shilatifard, A. (2016). Epigenetic balance of gene expression by Polycomb and
716 COMPASS families. Science *352*, aad9780.

717 Ramirez, F., Ryan, D.P., Gruning, B., Bhardwaj, V., Kilpert, F., Richter, A.S., Heyne, S., Dundar, F.,
718 and Manke, T. (2016). deepTools2: a next generation web server for deep-sequencing data analysis.
719 Nucleic Acids Res *44*, W160-165.

720 Robinson, J.T., Thorvaldsdottir, H., Winckler, W., Guttman, M., Lander, E.S., Getz, G., and Mesirov,
721 J.P. (2011). Integrative genomics viewer. Nat Biotechnol *29*, 24-26.

722 Robinson, J.T., Turner, D., Durand, N.C., Thorvaldsdottir, H., Mesirov, J.P., and Aiden, E.L. (2018).
723 Juicebox.js Provides a Cloud-Based Visualization System for Hi-C Data. Cell Syst *6*, 256-258 e251.

724 Ronan, J.L., Wu, W., and Crabtree, G.R. (2013). From neural development to cognition: unexpected
725 roles for chromatin. Nat Rev Genet *14*, 347-359.

726 Rose, N.R., King, H.W., Blackledge, N.P., Fursova, N.A., Ember, K.J., Fischer, R., Kessler, B.M., and
727 Klose, R.J. (2016). RYBP stimulates PRC1 to shape chromatin-based communication between
728 Polycomb repressive complexes. Elife *5*.

729 Schuettengruber, B., Bourbon, H.M., Di Croce, L., and Cavalli, G. (2017). Genome Regulation by
730 Polycomb and Trithorax: 70 Years and Counting. Cell *171*, 34-57.

731 Shain, A.H., and Pollack, J.R. (2013). The spectrum of SWI/SNF mutations, ubiquitous in human
732 cancers. PLoS One *8*, e55119.

733 Soneson, C., Love, M.I., and Robinson, M.D. (2015). Differential analyses for RNA-seq: transcript-level
734 estimates improve gene-level inferences. F1000Res *4*, 1521.

735 Stanton, B.Z., Chory, E.J., and Crabtree, G.R. (2018). Chemically induced proximity in biology and
736 medicine. Science *359*.

737 Stanton, B.Z., Hodges, C., Calarco, J.P., Braun, S.M., Ku, W.L., Kadoch, C., Zhao, K., and Crabtree,
738 G.R. (2017). Smarca4 ATPase mutations disrupt direct eviction of PRC1 from chromatin. Nat Genet *49*,
739 282-288.

740 Tamburri, S., Lavarone, E., Fernandez-Perez, D., Conway, E., Zanotti, M., Manganaro, D., and Pasini,
741 D. (2019). Histone H2AK119 Mono-Ubiquitination Is Essential for Polycomb-Mediated Transcriptional
742 Repression. Mol Cell.

743 Tamkun, J.W., Deuring, R., Scott, M.P., Kissinger, M., Pattatucci, A.M., Kaufman, T.C., and Kennison,
744 J.A. (1992). brahma: a regulator of Drosophila homeotic genes structurally related to the yeast
745 transcriptional activator SNF2/SWI2. Cell *68*, 561-572.

746 Tie, F., Banerjee, R., Stratton, C.A., Prasad-Sinha, J., Stepanik, V., Zlobin, A., Diaz, M.O., Scacheri,
747 P.C., and Harte, P.J. (2009). CBP-mediated acetylation of histone H3 lysine 27 antagonizes Drosophila
748 Polycomb silencing. Development *136*, 3131-3141.

749 Valencia, A.M., and Kadoch, C. (2019). Chromatin regulatory mechanisms and therapeutic
750 opportunities in cancer. Nat Cell Biol *21*, 152-161.

751 Wang, X., Paucek, R.D., Gooding, A.R., Brown, Z.Z., Ge, E.J., Muir, T.W., and Cech, T.R. (2017).
752 Molecular analysis of PRC2 recruitment to DNA in chromatin and its inhibition by RNA. Nat Struct
753 Mol Biol *24*, 1028-1038.

754 Wishart, D.S., Feunang, Y.D., Guo, A.C., Lo, E.J., Marcu, A., Grant, J.R., Sajed, T., Johnson, D., Li, C.,
755 Sayeeda, Z.*, et al.* (2018). DrugBank 5.0: a major update to the DrugBank database for 2018. Nucleic
756 Acids Res *46*, D1074-D1082.

757 Ying, Q.L., Wray, J., Nichols, J., Batlle-Morera, L., Doble, B., Woodgett, J., Cohen, P., and Smith, A.
758 (2008). The ground state of embryonic stem cell self-renewal. Nature *453*, 519-523.
759
760
761
762
763
764
765
766
767
768
769
770
771
772
773
774
775
776

Supplementary Figures:

Weber et al., Supplemental Figure 1

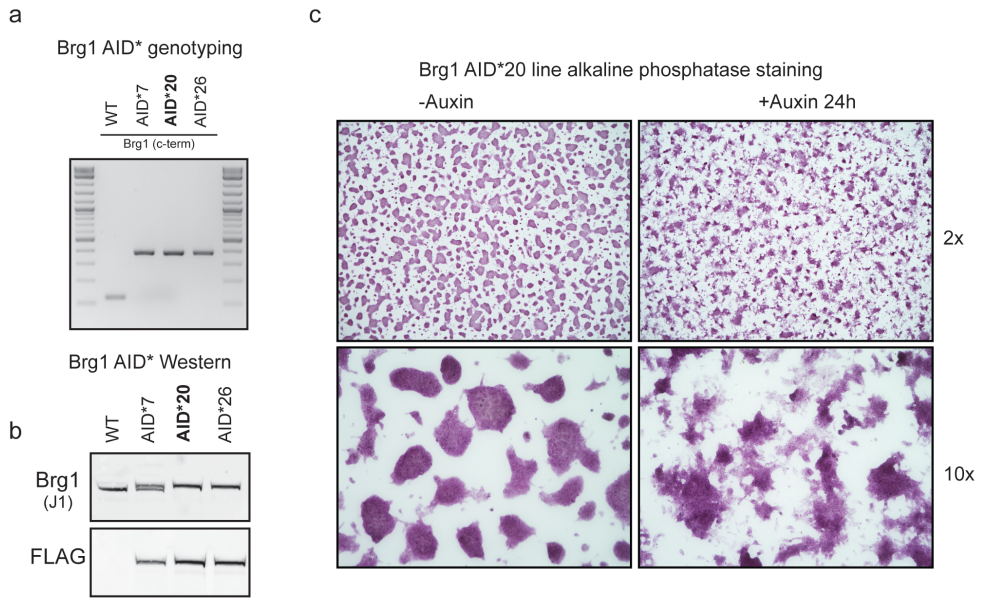

Supp. Fig 1 Extended characterization of Brg1 AID degron
(a) Genotyping PCR for three homozygous knock-in clones (AID*20 was used for most experiments in the manuscript). (b) Western blot of whole-cell extracts from knock-in lines showing 8.8kDa shift in migration from c-terminal tag (G4S)3-AID*-G4S-3xFLAG. Line 20 and 26 have homozygous insertion that is in the correct frame and was confirmed by Sanger sequencing. (c) Alkaline phosphatase staining of Brg1 AID* 20 line on gelatin coated dishes, +/- 24h auxin treatment to degrade Brg1.

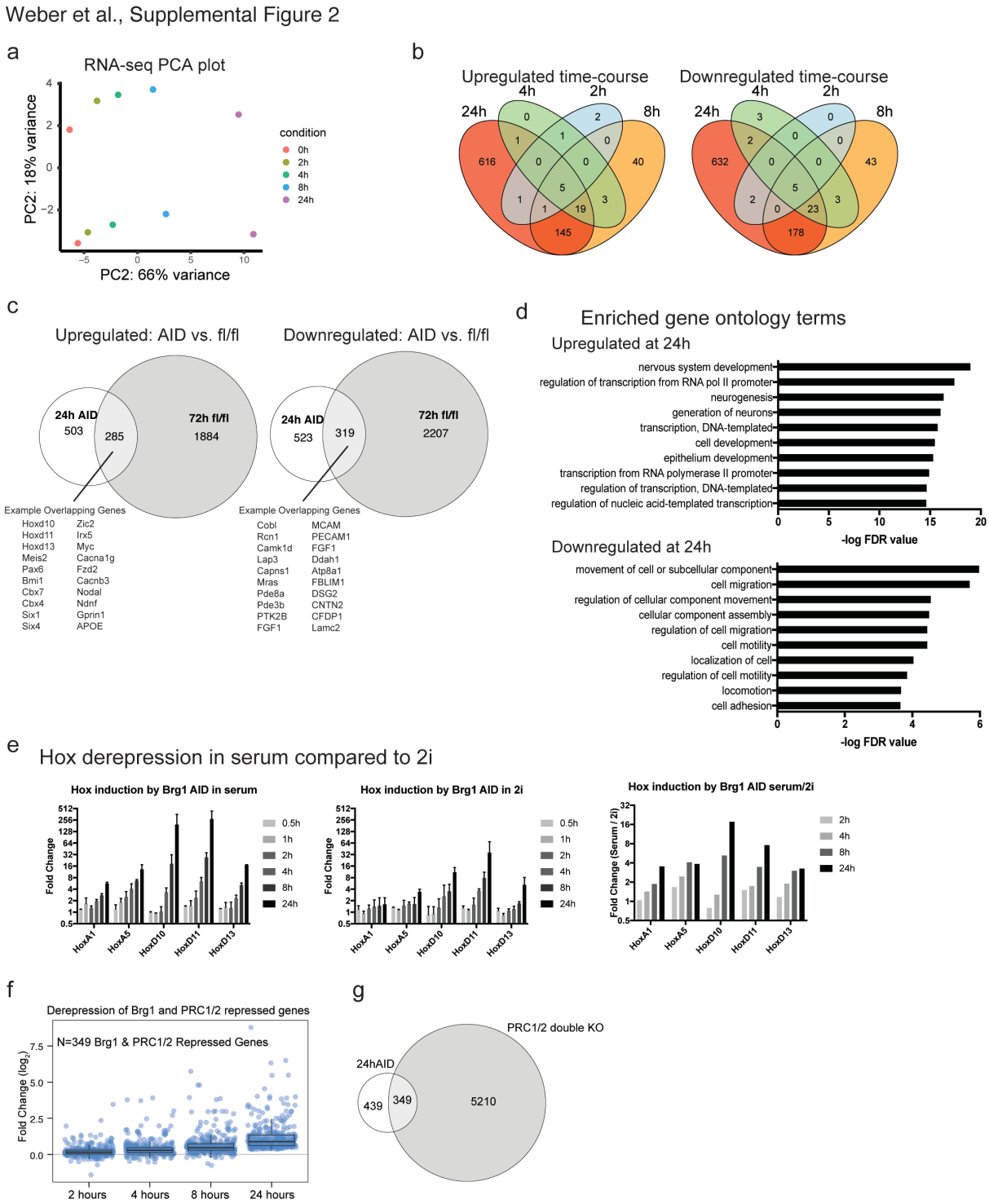

Supp. Fig 2 Extended summary of RNA-seq results, related to figure 2

(a) Principal component analysis of RNA-seq conditions and n = 2 replicates for each time-point. (b) Venn diagram showing the overlap of significantly upregulated and downregulated genes over the 2, 4, 8, and 24h time-course. (c) Venn diagram overlapping differentially expressed genes at 24h Brg1 AID and 72h cKO from at FDR-corrected P < 0.05(Stanton et al., 2017). (d) Enriched gene ontology terms for upregulated and downregulated genes as determined by DAVID. (e) Hox gene derepression measured by qRT-PCR for cells grown in serum, 2i, and the ratio of serum/2i. Error bars are mean +/- standard deviation from two biological replicates. (f) (top) Scatterplot of genes derepressed by Brg1 degradation at 24h and PRC1&2 cKO over the time-course. (g) Venn diagram depicting the overlap between 24h Brg1 degradation and PRC1&2 cKO. PRC1&2 cKO data is from Ring1$^{-/-}$;Rnf2$^{fl/fl}$;Eed$^{-/-}$ ESCs that were treated with TAM for 72h from (King et al., 2018).

Weber et al., Supplemental Figure 3

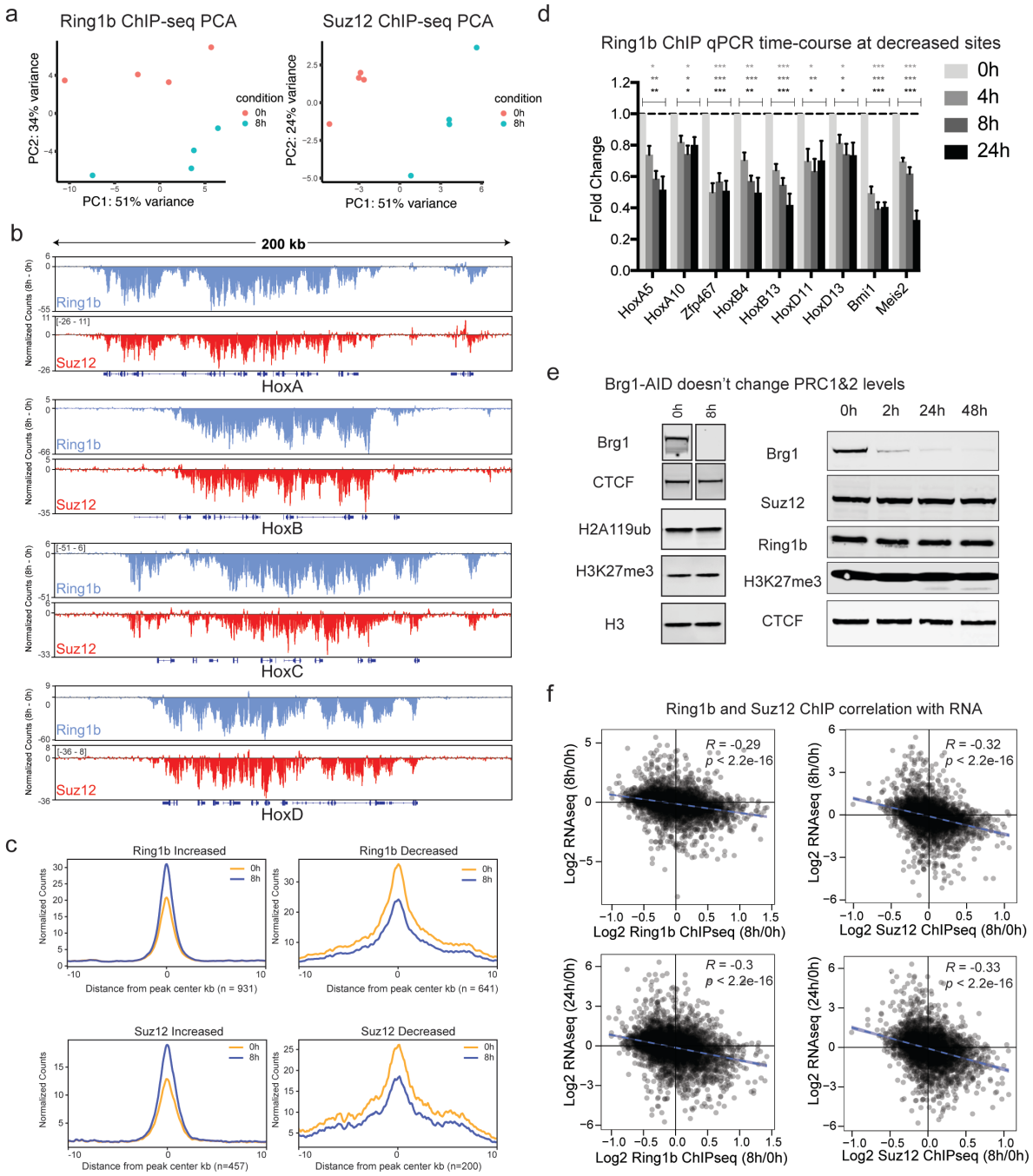

Supp. Fig 3 Brg1 degradation results in quick redistribution of PRC1&2 but doesn't affect net dosage, related to figure 3
(a) Principal component analysis of Ring1b and Suz12 ChIP-seq (n = 4 replicates) (b) Browser snapshot of the difference in normalized counts (8h – 0h) for Ring1b and Suz12 at Hox A, B, C, and D depicting net loss across all four clusters. (c) Average metagene plots of normalized counts (to read-depth) at sites that were significantly increased or decreased by DESeq2 analysis (FDR-corrected P < 0.1) and normalized to peak intensity, providing additional confirmation that normalization is correct. (d) ChIP qPCR time-course at 4, 8, and 24h Brg1 degradation for Ring1b at sites that were significantly decreased by ChIP-seq. Error bars depict standard error of the mean from four biological replicates. (* = p<0.05, ** = p<0.005, *** = p<0.0005; t test with Holm-Sidak multiple comparison correction). (e) (left) Representative western blot showing Brg1 degradation efficiency and that H2AK119ub and H3K27me3 marks don't change at 8h time-point (ChIP-seq time-point for the complexes that deposit these marks). (right) Representative western showing Brg1 degradation efficiency over a longer time-course and that Suz12, Ring1b, and H3K27me3 marks don't noticeably change even at 48h. (f) Correlation of all Ring1b and Suz12 peaks that are +/- 2kb from gene transcription start sites and expression changes at 8h Brg1 degradation. Correlation and p-values were obtained from Pearson's product moment correlation.

797

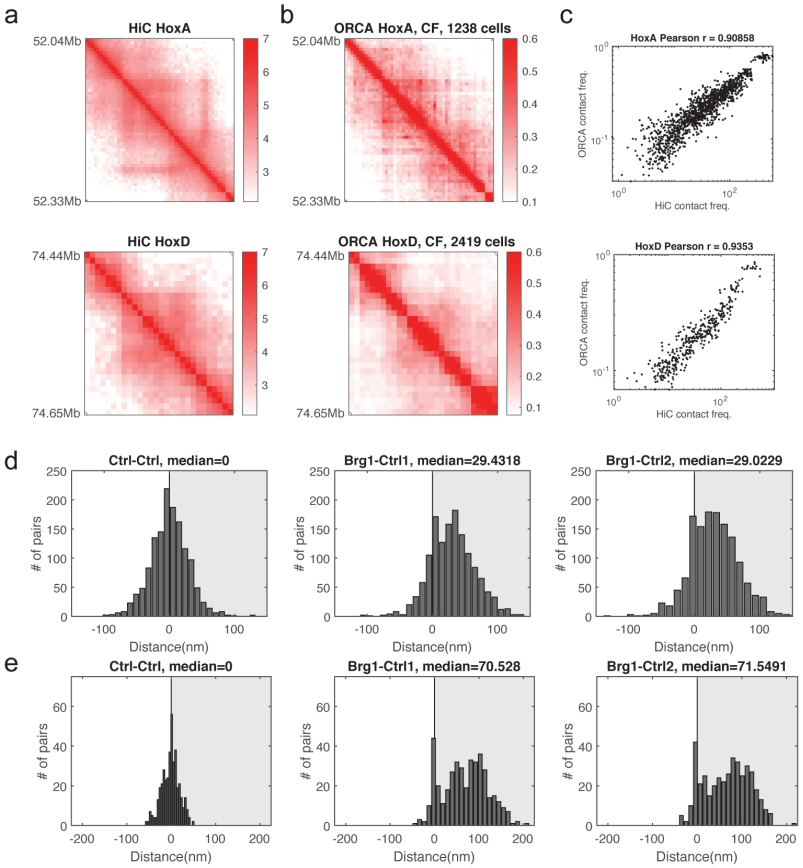

Supp. Fig 4 Comparison of ORCA to Hi-C, related to figure 4
(a) Average contact frequency as measured by high resolution Hi-C from (Bonev et al., 2017). (b) Average contact frequency as measured by ORCA (150-nm threshold). (c) Pearson's correlation and Pearson's r were computed using all unique pairwise combinations of X,Y barcodes measured. (d) Histograms depicting the difference in median distance for barcode pair combinations at HoxA. (e) Histograms depicting the difference in median distance for barcode pair combinations at HoxD.

Weber et al., Supplemental Figure 5

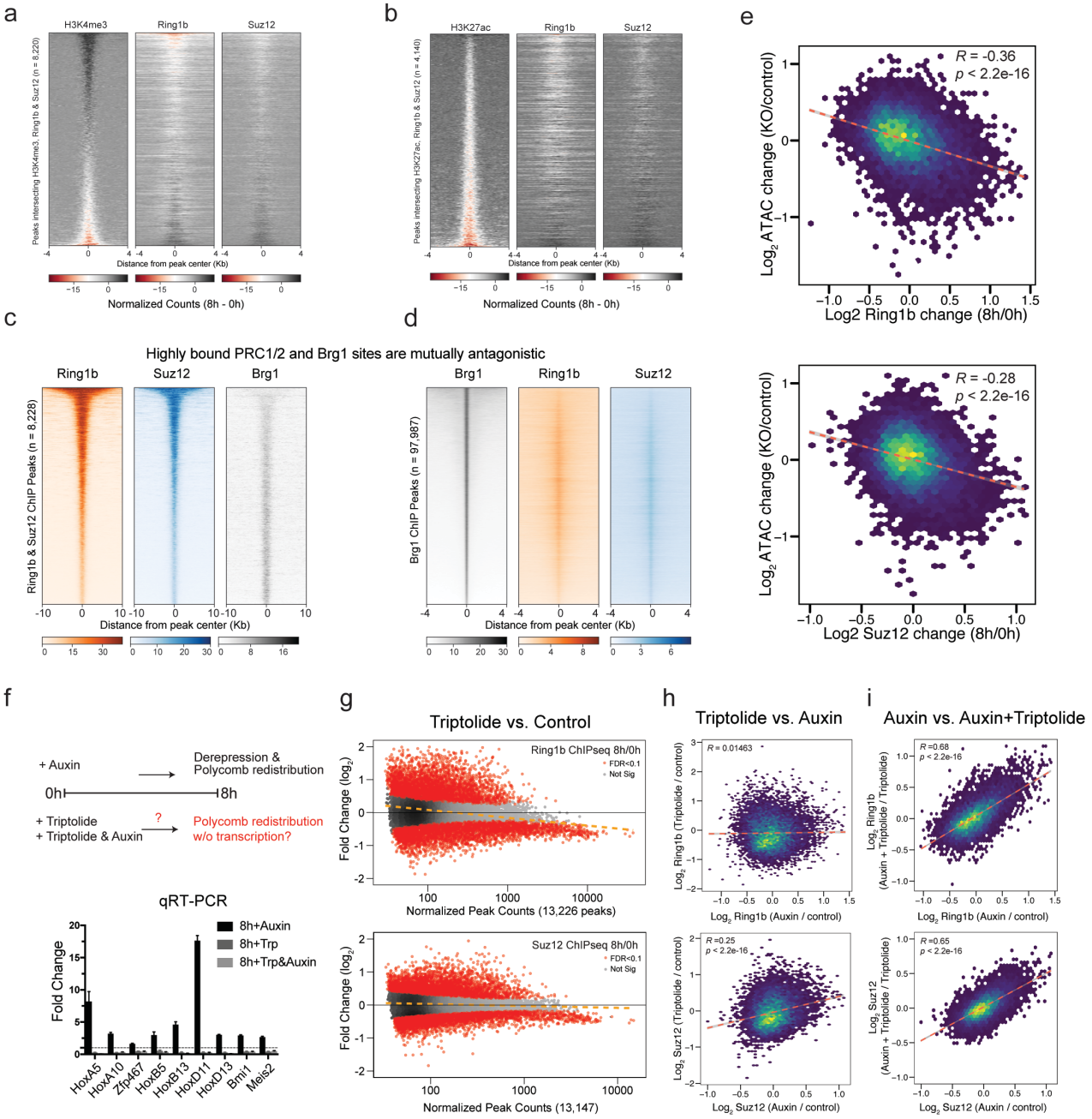

Supp. Fig 5 Extended analysis related to figure 5

(a) Heatmap depicting the negative correlation between H3K4me3 and Ring1b and Suz12 as the difference in normalized counts (8h – 0h) at peaks (8,220) that intersect H3K4me3, Ring1b, and Suz12 at merged peak center, sorted by decreasing H3K4me3 signal. (b) Heatmap depicting the negative correlation between H3K27ac and PRC1&2 as the difference in normalized counts (8h – 0h) at peaks (4,140) that intersect H3K27ac, Ring1b, and Suz12 at merged peak center, sorted by decreasing H3K27ac signal. (c) Heatmap depicting Ring1b, Suz12, and Brg1 signal from (Gatchalian et al., 2018) at peaks (8,228) that overlap for Ring1b and Suz12, sorted by decreasing Ring1b signal. (d) Heatmap depicting Brg1, Ring1b, and Suz12 signal at Brg1 peaks (97,987) sorted by decreasing Brg1 signal. (e) Scatterplots showing negative correlation between ATAC-seq changes (KO/control) (Miller et al., 2017) and Ring1b (8h/0h) or Suz12 (8h/0h). (f) Experimental design to test effect of inhibiting transcription initiation on polycomb redistribution. qRT-PCR depicting fold change by ΔΔCt method with indicated treatments. (g) MA plot showing genome-wide changes to Ring1b and Suz12 ChIP-seq peaks (n = 13,226 and n = 13,147 respectively) at 8h Triptolide / Control with bound peaks in red (FDR-corrected P < 0.1) from four biological replicates. (h) Scatterplot of changes to Ring1b and Suz12 upon treatment with auxin (auxin / control) or triptolide (triptolide / control) (i) Scatterplot of changes to Ring1b and Suz12 upon treatment with auxin (auxin / control) or auxin + triptolide (auxin + triptolide / triptolide). Correlation and p-values were obtained from Pearson's product moment correlation for e, h, and i.

803

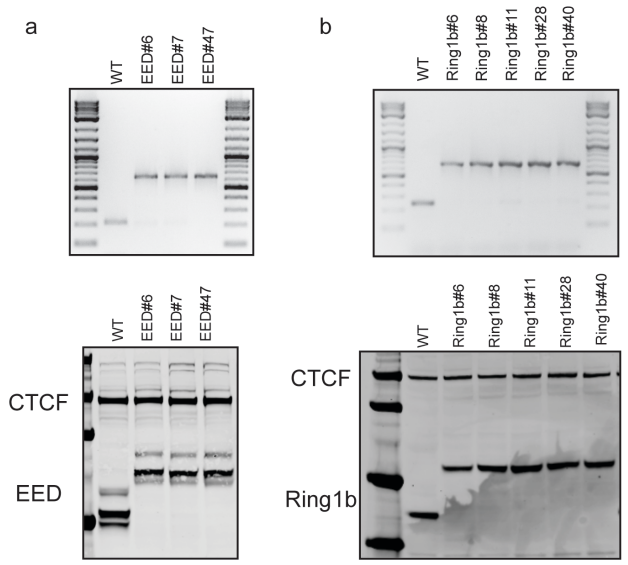

Supp. Fig 6 Extended characterization of Ring1b and EED dTAG lines in Figure 6.
(a) Genotyping PCR and western from WCE with 14.6kDa shift in migration from C-terminus (G4S)3-FKBP^{F36V}-G$_4$S-V5 tag on three different EED clones used for experiments. (b) Genotyping PCR and western from WCE with 14.2kDa shift in migration from N-terminus FKBP^{F36V}-G4S-HA-(G4S)3.

804

Weber et al., Table 1

Target	CW-number	sequence	assay	notes
GAPDH	CW03F_GAPDH	CGTCCCGTAGACAAAATGGT	qRTPCR	
GAPDH	CW03R_GAPDH	TTGATGGCAACAATCTCCAC	qRTPCR	
Hoxa1	235F-Hoxa1-a	CCACCAGGGTTATGCTGGG	qRTPCR	
Hoxa1	235R-Hoxa1-a	CGTGGAGAGGGGATAAGGAGTTA	qRTPCR	
Hoxa3	467F-HoxA3qRTPCR	AAGTGCCAACAGCAACCCTAC	qRTPCR	
Hoxa3	467R-HoxA3qRTPCR	AGGGAAAGATTTGTTTGCCCA	qRTPCR	
Hoxa5	219F-Hoxa5-b	AGGTAGCGGTTGAAGTGGAA	qRTPCR	
Hoxa5	220R-Hoxa5-c	GCTCAGCCCCAGATCTACC	qRTPCR	
Hoxa10	206F-Hoxa10	TCTTTGCTGTGAGCCAGTTG	qRTPCR	
Hoxa10	206R-Hoxa10	CTCCAGCCCCTTCAGAAAAC	qRTPCR	
Hoxb3	472F-HoxB3qRTPCR	GCTCAGAGGAGGGGAGATTT	qRTPCR	
Hoxb3	472R-HoxB3qRTPCR	GGGGAGAACAGGCAGACATA	qRTPCR	
Hoxb5	123F-Hoxb5-qRTPCR	CTGGTAGCGAGTATAGGCGG	qRTPCR	*sub for HoxB4
Hoxb5	123R-Hoxb5-qRTPCR	AGGGGCAGACTCCACAGATA	qRTPCR	*sub for HoxB4
Hoxb7	471F-HoxB7qRTPCR	GCCGCAAGTTCGGTTTTCG	qRTPCR	
Hoxb7	471R-HoxB7qRTPCR	GCAAAGGCGCAAGAAGTTTGT	qRTPCR	
Hoxb13	432F-HoxB13	GATGTGTTGCCAAGGTGAAC	qRTPCR	
Hoxb13	432R-HoxB13	CCTTGCTATAGGGAATGCGT	qRTPCR	
Hoxd10	197F-Hoxd10-qPCR	TCTCCTGCACTTCGGGAC	qRTPCR	
Hoxd10	197R-Hoxd10-qPCR	GGAGCCCACTAAAGTCTCCC	qRTPCR	
Hoxd11	229F-Hoxd11-b	AGGTTGAGCATCCGAGAGAG	qRTPCR	
Hoxd11	229R-Hoxd11-b	GAAAAAGCGCTGTCCCTACA	qRTPCR	
Hoxd13	196F-Hoxd13-qPCR	TGGTGTAAGGCACCCTTTTC	qRTPCR	
Hoxd13	196R-Hoxd13-qPCR	CCCATTTTTGGAAATCATCC	qRTPCR	
Bmi1	192F-Bmi1-qPCR	TACCATGAATGGAACCAGCA	qRTPCR	
Bmi1	192R-Bmi1-qPCR	AAAGGAAGCAAACTGGACGA	qRTPCR	
Meis2	437F-Meis2	GACCACAACCCTTCATCCTG	qRTPCR	
Meis2	437R-Meis2	TTGTCTAACCCATCGCCTTG	qRTPCR	
Pax6	438F-Pax6	CCCTCACCAACACGTACAG	qRTPCR	
Pax6	438R-Pax6	TCATAACTCCGCCCATTCAC	qRTPCR	
U6	440F-U6snRNA	CGCTTCGGCAGCACATATAC	qRTPCR	
U6	440R-U6snRNA	TTCACGAATTTGCGTGTCAT	qRTPCR	
HoxA5	266F-PRC12-pkE	GCTGGAGAGAGGCGAGACTA	ChIP_qPCR	
HoxA5	266R-PRC12-pkE	GTAAAGCCAGCCGTTTTCTG	ChIP_qPCR	
HoxA10	265F-PRC12-pkD	GTCGACCAAAAAGGAGTTCG	ChIP_qPCR	
HoxA10	265R-PRC12-pkD	TGTCAGCCAGAAAGGGCTAT	ChIP_qPCR	
Zfp467	394F-Zfp467-A	GCAGCCGAGTAAGTGGTAGC	ChIP_qPCR	
Zfp467	394R-Zfp467-A	TGACCGATTCTCCCAATCTC	ChIP_qPCR	
HoxB4	417F-HoxB4-D	AGGGAGTGTTGAGGAGGACA	ChIP_qPCR	
HoxB4	417R-HoxB4-D	GCGAGCAGATCGATAGGAAA	ChIP_qPCR	
HoxB13	418F-HoxB13-A	AACACGCATGTGAAAGTGGA	ChIP_qPCR	
HoxB13	418R-HoxB13-A	CTCACACCAGGAGTCTGCAA	ChIP_qPCR	
HoxD11	263F-PRC12-pkB	GAACAGAGCGGAAAAACCTG	ChIP_qPCR	

HoxD11	263R-PRC12-pkB	AGAGTGCAGACCCTGGAAAA	ChIP_qPCR	
HoxD13	264F-PRC12-pkC	GGGTGACGCGGTAGACTAAG	ChIP_qPCR	
HoxD13	264R-PRC12-pkC	GCACACCAAAGTGAGGATGA	ChIP_qPCR	
Bmi1	269F-PRC12-pkH	CGCCCTTTGTTGAGAGGTAG	ChIP_qPCR	
Bmi1	269R-PRC12-pkH	ACCTCCAGAGCCCTTTCTTC	ChIP_qPCR	
Meis2	409F-Meis2-D	GCTCGCACTTCTCAAAAACC	ChIP_qPCR	
Meis2	409R-Meis2-D	GTTCTTGCTCCTTCCCCTCT	ChIP_qPCR	

Weber et al., Table 2

Antibody	**Source**	**Identifier**
Rabbit monoclonal anti-Ring1b (ChIP & WB)	CST	Cat #5694; RRID:AB_10705604
Rabbit polyclonal anti-Suz12 (ChIP & WB)	Active Motif	Cat #39057; RRID:AB_2614929
Rabbit polyclonal to Histone H3 (acetyl K27) (ChIP)	Abcam	Cat#ab4729
Rabbit polyclonal to Histone H3 (trimethyl K27) (WB)	Active Motif	Cat#39155; RRID:AB_2561020
Rabbit monoclonal to Histone H3 (trimethyl K4) (ChIP)	Sigma	Cat#04-745
Rabbit monoclonal to CTCF (WB)	Abcam	Cat#ab128909
Mouse monoclonal to Brg1 (WB)	Santa Cruz	Cat#sc-374197
Rabbit polyclonal to EED (WB)	CST	Cat#51673
Rabbit monoclonal to Histone H2A (ub K119) (WB)	CST	Cat#8240
Mouse monoclonal to Histone H3 (WB)	CST	Cat#3638
Rabbit polyclonal to PCGF1	Sigma	Cat#HPA11356